

The Geometry of Machine Learning Models*

Pawel Gajer^{1†} and Jacques Ravel¹

¹Center for Advanced Microbiome Research and Innovation (CAMRI),
Institute for Genome Sciences, and Department of Microbiology and Immunology,
University of Maryland School of Medicine

Abstract

This paper presents a mathematical framework for analyzing machine learning models through the geometry of their induced partitions. By representing partitions as Riemannian simplicial complexes, we capture not only adjacency relationships but also geometric properties including cell volumes, volumes of faces where cells meet, and dihedral angles between adjacent cells. For neural networks, we introduce a differential forms approach that tracks geometric structure through layers via pullback operations, making computations tractable by focusing on data-containing cells. The framework enables geometric regularization that directly penalizes problematic spatial configurations and provides new tools for model refinement through extended Laplacians and simplicial splines. We also explore how data distribution induces effective geometric curvature in model partitions, developing discrete curvature measures for vertices that quantify local geometric complexity and statistical Ricci curvature for edges that captures pairwise relationships between cells. While focused on mathematical foundations, this geometric perspective offers new approaches to model interpretation, regularization, and diagnostic tools for understanding learning dynamics.

Keywords: Geometric deep learning, Neural network geometry, Discrete Riemannian geometry, Model interpretability, Geometric regularization, Discrete differential geometry

1 Introduction

Modern machine learning models achieve remarkable empirical success, yet their internal mechanisms remain largely opaque. While theoretical foundations have evolved from early function approximation results [23, 39] to include geometric perspectives such as neural tangent kernels [40], loss landscape analysis [47], and geometric deep learning [18], these

*Research reported in this publication was supported by grant number INV-048956 from the Gates Foundation.

[†]Corresponding author: pgajer@gmail.com

approaches have not systematically characterized how models partition their input spaces and the geometric properties of these partitions. Similarly, while interpretability methods have progressed beyond pure input-output analysis to include feature visualization [53] and representation probing [2, 7], they typically do not examine the spatial organization of decision regions—how cells meet, their relative volumes, and the angles at which boundaries intersect. Performance metrics provide precise measurements of accuracy but incomplete explanations for why certain architectural and training choices lead to better generalization [73, 51]. This opacity becomes particularly problematic when deploying models in critical applications where understanding failure modes is paramount [58, 27].

This paper develops a framework that analyzes machine learning models through their inherent geometric structures. Many successful methods, including decision trees [17], multivariate adaptive regression splines [31], random forests [16], gradient boosting [32], and neural networks [45, 33], fundamentally operate by partitioning their input space into regions. These partitions possess geometric properties including cell volumes, volumes of faces where cells meet, and dihedral angles between adjacent cells that provide a new lens for understanding model behavior.

The mathematical framework we develop represents machine learning models as simplicial complexes, establishing a geometric interpretation that applies across diverse model classes. Simplicial complexes provide a natural way to encode not just which regions are adjacent (as in a graph), but how multiple regions meet simultaneously, information that graphs cannot capture. When four decision tree cells meet at a point, or when three neural network regions share a common boundary, these higher-order relationships contain geometric information essential for understanding model behavior.

Through the nerve construction [12], any partition transforms into a simplicial complex where vertices represent regions, edges capture adjacency, and higher-dimensional simplices encode multi-way intersections. Decision trees create axis-aligned partitions whose simplicial complexes have a characteristic structure: each point where 2^n cells meet (in n dimensions) corresponds to a $(2^n - 1)$ -dimensional simplex in the nerve complex. Ensemble methods generate overlapping partitions that must be carefully reconciled, with each base model contributing its own partition structure. The reconciled partition then induces a single simplicial complex that captures the ensemble’s combined geometry. For neural networks, we analyze their structure through refined partitions: as data flows through layers, we track how cells subdivide and map between layers, constructing functionally enriched simplicial complexes that capture both the combinatorial adjacency relationships and the affine transformations within each region.

The framework equips these simplicial complexes with a Riemannian structure through inner products on chain spaces that encode the geometric properties of partitions: cell volumes, face volumes, and dihedral angles in a mathematically precise way. For neural networks specifically, we employ a differential forms approach where volumes and boundary measures transform systematically under pullback operations through the layers, yielding explicit formulas that reduce geometric computations from potentially exponentially many cell intersections to calculations on only cells that actually contain training data. This provides a geometric characterization of deep networks that goes beyond simply noting their piecewise linear structure.

Our geometric framework complements but differs from existing approaches like persistent homology [19, 28], which studies topological features of data, and manifold learning [61, 57], which seeks low-dimensional representations. Rather than analyzing data geometry, we study the geometry of model-induced partitions, revealing how learning algorithms organize and navigate feature space.

The geometric framework enables regularization strategies that directly target spatial properties associated with good generalization. While traditional regularization operates indirectly by limiting tree depth or penalizing weight magnitudes [63, 75], geometric regularization directly penalizes problematic spatial configurations: extreme volume disparities between regions, sharp angles at boundaries, or excessive fragmentation.

Beyond regularization, the geometric framework enables new approaches to model refinement. We introduce extended Laplacians that incorporate higher-order simplicial information, moving beyond traditional graph-based smoothing to respect the full geometric structure of how cells meet in space. We also develop simplicial splines that extend classical spline regression to high-dimensional data by leveraging the Riemannian simplicial complex structure, avoiding the limitations of tensor product approaches while respecting the partition geometry. These tools offer new ways to smooth and refine the piecewise constant predictions of partition models while respecting their inherent geometric structure.

This geometric perspective also suggests new directions for understanding machine learning. We introduce density-weighted metrics on the simplicial complexes that incorporate the distribution of training data, making paths through high-density regions effectively shorter than those through sparse regions. This enriched geometric structure captures how data concentration affects model behavior and provides new tools for analyzing generalization.

A key insight of our framework is that real-world data, despite living in high-dimensional Euclidean space, is typically sparse and highly structured. This sparsity and non-uniform distribution effectively creates geometric curvature. When data concentrates in specific regions or along lower-dimensional structures while leaving vast regions empty, machine learning models must adapt their partitions to this inhomogeneous structure. The resulting geometry exhibits curvature-like properties that our framework can measure and quantify.

This observation leads to concepts that extend classical differential geometry to the real-world data setting. We develop statistical curvature measures that quantify local geometric complexity through multiple approaches: ball-growth curvature that measures how density-weighted neighborhoods expand, geodesic spreading that tracks path divergence, and functional curvatures that capture how model predictions vary across the partition. Building on these vertex-based measures, we introduce statistical Ricci curvature for edges that combines geometric, density, and functional components. This edge-based curvature captures relational properties between cells that vertex measures alone cannot detect, enabling a more complete geometric characterization of model behavior.

The curvature framework provides practical tools for model analysis and improvement. We develop geometric regularization that penalizes extreme curvatures at both vertices and edges, encouraging models with balanced geometric structure. For monitoring learning dynamics, we track how curvature distributions evolve during training, potentially revealing transitions from learning robust patterns to overfitting. These geometric diagnostics complement traditional loss-based metrics, offering new insights into model behavior.

While this paper focuses on developing the mathematical foundations, the geometric framework opens several avenues for practical impact. The geometric regularization methods could lead to models with better interpretability and more predictable failure modes. The ability to quantify geometric properties like cell volumes and boundary angles provides new diagnostic tools for understanding when and why models overfit. For practitioners, the framework offers a principled approach to comparing architectures based on their induced geometric structures rather than solely on performance metrics. Experimental validation of these theoretical insights remains an important direction for future work.

The rest of the paper is organized as follows. Section 2 introduces the geometric framework through partition models, where the connection between model structure and induced geometry appears most directly. We begin with decision trees and their natural simplicial complexes, extend to ensemble methods that create overlapping partitions, and develop the theory of geometric regularization. Section 2.4 explores the incorporation of statistical structure through density-weighted metrics and the emergence of curvature-like phenomena, developing both vertex-based and edge-based curvature measures along with their applications to regularization and model monitoring. Section 3 extends the framework to neural networks, showing how layer-wise computation induces sequences of simplicial complexes with rich geometric structure.

2. Partition Models

Partition-based machine learning models, from decision trees to their powerful ensemble extensions, have become fundamental tools in modern data analysis. These models succeed by dividing the feature space into regions, each associated with a local prediction. Yet despite their widespread use and empirical success, we have limited tools for understanding and improving the geometric structures these partitions create.

Consider the spatial patterns that emerge when a decision tree recursively splits a feature space. Some regions may become extremely small to accommodate individual training points, while others span large volumes. Boundaries between regions follow axis-aligned or linear cuts that may create jagged, indirect paths between naturally connected areas. These geometric properties, including cell volumes, boundary configurations, and angles at which regions meet, contain rich information about model behavior that current methods largely ignore.

What if we could systematically analyze these geometric structures? Rather than treating partitions merely as computational byproducts, we can view them as geometric objects amenable to mathematical analysis. This perspective opens new avenues: detecting when a model creates unnecessarily complex spatial structures, identifying opportunities for smoothing without sacrificing predictive power, and developing principled approaches to combine multiple partitions in ensembles.

This section develops a geometric framework for understanding partition-based models through the lens of Riemannian simplicial complexes. We begin by reviewing how various machine learning models create partitions and their current regularization strategies (Section 2.1). We then introduce a geometric perspective that captures not just which cells are

adjacent but how they meet in space (Section 2.2). This framework enables novel analysis tools and regularization approaches that directly leverage spatial structure. Finally, we demonstrate how this geometric understanding leads to principled model refinement techniques using simplicial splines and extended Laplacians (Section 2.3).

2.1 Partition Models in Machine Learning

How do machine learning models make sense of complex, high-dimensional data? One of the most successful strategies involves dividing the feature space into manageable regions, with each region receiving its own tailored prediction. A decision tree examining house prices might separate urban from suburban properties, then further divide based on square footage, creating a hierarchy of increasingly specific regions. Each leaf of the tree corresponds to a subset of the feature space where houses share similar characteristics and, presumably, similar prices.

This divide-and-conquer approach appears throughout machine learning. Random forests combine hundreds of such partitions to achieve remarkable predictive power. Multivariate adaptive regression splines create smooth transitions between regions while maintaining the essential piecewise structure. Support vector machines with local models adapt their decision boundaries to regional data characteristics. What unites these diverse methods is their fundamental operation: partitioning the feature space and assigning local models to each piece.

Yet despite their empirical success, we lack a unified framework for understanding these partition-based models. What geometric principles govern effective partitions? When a model creates hundreds of tiny regions to fit training data, how can we distinguish necessary complexity from overfitting? How should adjacent regions relate to each other geometrically? These questions motivate a systematic study of partition models through the lens of geometry.

To establish this geometric perspective, we first formalize the notion of a partition model. Given observations $x_1, x_2, \dots, x_N \in \mathbb{R}^n$ and responses $y_1, y_2, \dots, y_N \in \mathbb{R}$, a partition model constructs a decomposition of the feature space into regions, each associated with a local prediction function. Formally, the model defines a partition $\mathcal{P} = \{C_\alpha\}_\alpha$ of a domain $\mathcal{D} \subset \mathbb{R}^n$, where \mathcal{D} is typically chosen as the smallest axis-aligned hyperrectangle containing all observed data points. The cells C_α satisfy the covering and disjointness properties:

$$\bigcup_{\alpha} C_{\alpha} = \mathcal{D}, \quad C_{\alpha}^{\circ} \cap C_{\alpha'}^{\circ} = \emptyset \text{ for } \alpha \neq \alpha',$$

where C° denotes the interior of cell C . Let I denote the set of indices α such that cell C_{α} contains at least one observation from $\{x_1, x_2, \dots, x_N\}$. While the partition may generate numerous cells covering the entire domain \mathcal{D} , the model considers only those cells indexed by I . This distinction is crucial: a decision tree might partition \mathcal{D} into thousands of regions, but only the subset containing training data influences the model's predictions and parameters. Each cell C_{α} with $\alpha \in I$ is associated with a local prediction function $f_{\alpha} : C_{\alpha} \rightarrow \mathbb{R}$. These functions are determined by minimizing an objective function that

typically includes a data fidelity term and may incorporate regularization:

$$\mathcal{L} = \sum_{\alpha \in I} \left(\sum_j \|f_{\alpha}(x_{\alpha,j}) - y_{\alpha,j}\|^2 + R_{\alpha} \right),$$

where $x_{\alpha,j}$ are the data points falling within C_{α} , $y_{\alpha,j}$ are their associated responses, and R_{α} represents an optional regularization term. When present, R_{α} may reflect the complexity of f_{α} , geometric properties of the cell, or structural constraints of the model class. Many partition models, particularly those with inherent structural constraints such as constant predictions within cells, may not require explicit regularization terms, setting $R_{\alpha} = 0$.

This formal framework encompasses a rich variety of machine learning methods, each making different choices about how to create partitions and what functions to use within each cell. Understanding these choices and their geometric implications forms the foundation for our subsequent analysis.

2.1.1 Common Partition Models

How do different machine learning algorithms create their partitions, and what geometric structures result from their choices? When we examine a trained decision tree, we see axis-aligned boxes dividing the feature space. A nearest neighbor classifier implicitly creates Voronoi cells around training points. A multivariate adaptive regression spline maintains smooth transitions across piecewise boundaries. These diverse geometric structures arise from fundamentally different partition strategies, yet we lack a unified way to compare and analyze them.

Understanding these geometric differences matters for practical model selection. What determines the magnitude of improvement when moving from a single decision tree to a random forest? How do the axis-aligned partitions of trees compare to the radial partitions of RBF networks in capturing different data patterns? By examining the partition structures created by various models, we can begin to understand their inductive biases and predict when each approach will excel.

The most familiar examples of partition models are tree-based methods [17, 35]. In regression and classification trees, the domain \mathcal{D} is recursively divided through axis-aligned splits of the form $x^{(j)} \leq t$. Each split introduces a hyperplane $x^{(j)} = t$ that partitions the current region into two subregions, ultimately producing hyperrectangular cells. Within each cell C_{α} , the prediction function is typically constant: $f_{\alpha}(x) = c_{\alpha}$. For regression, c_{α} is the average of response values in the cell; for classification, it is often the modal class or a probability vector over classes.

Multivariate Adaptive Regression Splines (MARS) [31] construct axis-aligned hyperrectangular partitions through products of hinge functions. A MARS model takes the form $f(x) = \beta_0 + \sum_{m=1}^M \beta_m B_m(x)$, where each basis function B_m is a product of terms $(x^{(j)} - t)_+ = \max(0, x^{(j)} - t)$ or $(t - x^{(j)})_+$. This construction implicitly partitions the domain into cells where f has a fixed polynomial form. Unlike tree methods, MARS enforces continuity across cell boundaries: for adjacent cells C_{α} and C_{β} , we have $\lim_{x \rightarrow x'} f(x) = \lim_{x \rightarrow x'} f(x)$

for $x' \in \partial C_\alpha \cap \partial C_\beta$. This combination of piecewise polynomial structure and continuity constraints distinguishes MARS as a smooth approximation method despite its partition-based foundation.

Oblique decision trees [50] generalize the partition structure beyond axis-aligned boundaries by allowing splits based on linear combinations of features. An internal node performs a test of the form $\beta^T x \leq t$, where $\beta \in \mathbb{R}^n$ is a weight vector not restricted to coordinate directions. This leads to partitions by arbitrarily oriented hyperplanes, resulting in general convex polyhedral cells rather than hyperrectangles. The prediction functions within each cell are typically constant, though more expressive variants with piecewise linear models have been developed [8].

Voronoi tessellations provide another approach to creating convex polyhedral partitions, based on proximity to prototype points rather than sequential splitting. Given prototypes $\mu_1, \dots, \mu_K \in \mathcal{D}$, the Voronoi cell C_k is defined as:

$$C_k = \{x \in \mathcal{D} : \|x - \mu_k\| \leq \|x - \mu_j\| \text{ for all } j \neq k\}.$$

Under the Euclidean norm, this yields convex polygonal or polyhedral cells whose boundaries are perpendicular bisectors between prototype pairs. Local prediction models within each cell range from constants (as in nearest neighbor methods [21]) to linear or nonlinear functions (as in local regression [20]). Vector quantization [34] and learning vector quantization [43] adaptively update the prototypes to optimize the partition for prediction accuracy.

Support vector machines with local models [14] implement partitioning through a two-stage process: first subdividing the feature space using clustering or other heuristics, then fitting an SVM within each region. These partitions can employ hard boundaries with distinct regions or soft transitions with overlapping influence functions, allowing adaptation to heterogeneous data distributions where global models fail to capture local patterns.

Recursive partitioning methods [74] provide a unifying framework that encompasses many of the approaches above. These methods divide the feature space recursively using flexible splitting criteria: single variables (axis-aligned trees), linear combinations (oblique trees), or more complex functions. The partition refinement continues until a stopping criterion is met, such as minimum cell occupancy or lack of improvement in prediction accuracy. This framework highlights how different choices of splitting functions and local models lead to the variety of partition-based methods in practice.

While recursive partitioning methods typically proceed top-down from a single cell containing all data, bottom-up approaches offer an alternative construction principle. These methods begin with a fine-grained partition and iteratively merge adjacent cells based on optimality criteria. For instance, one could initialize with a Voronoi tessellation using all data points as prototypes, then repeatedly merge adjacent cells when the merged predictor achieves lower error than the individual cells. This approach generalizes hierarchical clustering by replacing Ward’s variance-minimization criterion with a prediction-based merging criterion that directly optimizes model performance. Similar principles appear in region growing algorithms from image segmentation [1] and agglomerative information bottleneck methods [59], though adapted here for supervised learning with explicit local prediction functions. Such agglomerative methods naturally incorporate local geometry through the

adjacency structure and can discover partitions that balance model complexity with predictive accuracy. The choice between top-down splitting and bottom-up merging reflects different inductive biases: splitting emphasizes global structure and interpretability, while merging captures local similarities and can adapt to varying data density.

The partition models described above exhibit a progression in geometric and functional complexity. Axis-aligned methods (trees, MARS) create hyperrectangular cells that align with coordinate axes, facilitating interpretation but potentially requiring many cells for diagonal boundaries. General linear methods (oblique trees, Voronoi tessellations) allow arbitrary convex polyhedral cells, better adapting to data geometry at the cost of interpretability. Local model complexity ranges from constants through polynomials to general nonlinear functions, while continuity properties vary from the discontinuous predictions of trees to the smooth transitions of MARS and kernel-based methods. These structural differences directly influence the structure of the induced simplicial complexes, as explored in subsequent sections.

2.1.2 Regularization in Partition Models

Why do partition models with excellent training accuracy often fail catastrophically on new data? A decision tree might create thousands of tiny cells to perfectly classify training points, yet misclassify simple test cases. Current regularization approaches limit tree depth or penalize the number of leaves, but these constraints address symptoms rather than causes. The real problem lies deeper: pathological geometric structures that we cannot detect or penalize with existing methods.

Consider a partition where one cell occupies 99% of the feature space while hundreds of tiny cells fragment the remaining 1%. Traditional regularization counts each cell equally, missing this extreme imbalance. Or imagine cells meeting at sharp, knife-like angles that create unstable decision boundaries. Standard penalties on model complexity fail to distinguish this problematic geometry from a well-balanced partition with the same number of cells. These limitations suggest we need regularization approaches that directly target geometric properties.

Regularization in partition models serves to control model complexity and prevent overfitting, yet the form of the penalty R_α varies substantially across model classes. In tree-based methods, regularization typically constrains tree complexity through structural constraints rather than explicit penalty terms. Cost-complexity pruning adds a penalty term $\alpha|T|$ to the empirical loss, where $|T|$ denotes the number of terminal nodes. This can be interpreted as assigning a uniform regularization cost $R_\alpha = \alpha$ to each leaf cell, discouraging excessively deep trees [17].

For MARS models, regularization penalizes both the number of basis functions and their interaction complexity. The penalty typically takes the form

$$R_{\text{MARS}} = \lambda_1 M + \lambda_2 \sum_{m=1}^M d_m,$$

where M is the number of basis functions and d_m denotes the number of distinct variables in the m -th basis function, reflecting its interaction order [31, 35]. This formulation

discourages both model size and high-order interactions, promoting interpretability while controlling variance.

Similar limitations appear across other partition methods. Voronoi-based approaches typically regularize only the number or positions of prototype points, without considering the geometry of the resulting cells [43]. Oblique trees typically focus on finding optimal linear combinations for splits without explicit geometric regularization of the resulting partition structure [50, 37]. Support vector machines with local models often inherit regularization from their constituent SVMs, focusing on margin maximization within cells rather than the quality of the partition structure itself [14].

Classical regularization approaches thus target either the number of cells or the smoothness of functions within them, but rarely leverage the geometric structure of the partition. This limitation becomes apparent when considering pathological partitions: a model might create cells with extreme volume disparities, indicating potential overfitting to sparse data regions, or generate boundaries meeting at sharp angles, suggesting non-smooth decision surfaces that may generalize poorly. A partition with large surface-area-to-volume ratios might indicate excessive complexity, fragmenting the feature space unnecessarily.

These observations motivate the development of geometric regularization approaches that directly leverage the spatial properties of partitions, including natural geometric quantities such as cell volumes, boundary areas, and angles between adjacent cells.

2.2 Geometry of Partition Models

When two cells in a partition meet along a boundary, what geometric information does this relationship contain? Consider two adjacent regions created by a decision tree. We know they share a boundary, but we might also ask: How large is this shared boundary? Does a long boundary indicate a gradual transition while a small one suggests an abrupt change? If we compare the volumes of these cells, does a large disparity signal that one region is overly specialized? These questions reveal that partitions contain geometric information beyond mere adjacency.

The situation becomes richer when three or more cells meet at a point. The angles at which they meet encode information about the local configuration that pairwise relationships cannot capture. These geometric properties, such as boundary areas, cell volumes, and meeting angles, provide insights into model behavior that current regularization approaches overlook.

This section develops a mathematical framework to capture and exploit these geometric structures. We begin by showing how partitions naturally give rise to simplicial complexes that encode adjacency relationships (Section 2.2.1). We then enrich these structures with geometric information through Riemannian metrics (Section 2.2.2). This framework extends naturally to ensemble methods and reveals gradient boosting as a geometric flow (Sections 2.2.3-2.2.4). Finally, we demonstrate how these geometric insights enable new regularization strategies (Section 2.2.5).

2.2.1 From Partitions to Simplicial Complexes

How can we mathematically capture the relationships between cells in a partition beyond simple adjacency? When three or more cells meet at a point, they form a configuration that pairwise adjacency cannot describe. In three dimensions, four cells might meet at a vertex, creating a tetrahedral arrangement. The angles and orientations of this meeting contain geometric information essential for understanding the partition’s structure, yet standard graph representations discard these higher-order relationships.

This limitation affects the analysis of partition models and may impact the predictive performance of the partition model. A graph tells us which cells are neighbors but not how they meet in space. Are the cells arranged symmetrically around their common vertex, or do they form sharp, unstable configurations? Do many cells crowd together in one region while others stand isolated? These geometric patterns may impact model behavior and generalization, but we need richer mathematical structures to detect and quantify them.

To understand how geometric relationships in partitions can be captured mathematically, we begin with a familiar example: the relationship between Voronoi diagrams and Delaunay triangulations. Given points $X = \{x_1, x_2, \dots, x_k\}$ in \mathcal{D} , the Voronoi tessellation [67, 5] partitions \mathcal{D} into cells, where each cell C_i consists of all points closer to x_i than to any other point in X . This partition has a natural adjacency structure: two cells C_i and C_j are adjacent when they share a common boundary of dimension $n - 1$. The Delaunay triangulation [24] captures this adjacency by connecting points x_i and x_j with an edge whenever their corresponding Voronoi cells are adjacent.

This construction extends beyond edges. When three Voronoi cells in \mathbb{R}^2 meet at a common vertex, their generating points form a triangle in the Delaunay triangulation. More generally, whenever $d + 1$ Voronoi cells share a common face of dimension $n - d$, their generating points form a d -simplex in the Delaunay triangulation [52, 56]. The result is a simplicial complex that encodes the full combinatorial structure of the Voronoi partition.

The Delaunay triangulation exhibits a crucial property: if we have a triangle with vertices $\{x_i, x_j, x_k\}$, then we also have all three edges $\{x_i, x_j\}$, $\{x_i, x_k\}$, and $\{x_j, x_k\}$, as well as all three vertices. Similarly, a tetrahedron includes all its triangular faces, edges, and vertices. This closure property characterizes the structure of a simplicial complex. Formally, a simplicial complex on a vertex set V is a collection $K = \bigcup_{p=0}^d K_p$, where each K_p consists of $(p + 1)$ -element subsets of V called p -simplices [49, 36]. The defining property is closure under taking subsets: if $\sigma \in K$ and $\tau \subseteq \sigma$, then $\tau \in K$. This ensures that the boundary of every simplex is contained in the complex, guaranteeing that simplicial complexes have no self-intersections and maintain a coherent combinatorial structure.

The key insight is that this process applies to any partition, not just Voronoi tessellations. Given any partition $\mathcal{P} = \{C_\alpha\}_{\alpha \in I}$ of a bounded domain $\mathcal{D} \subseteq \mathbb{R}^n$, we associate each cell C_α with a vertex v_α , yielding vertex set $V = \{v_\alpha : \alpha \in I\}$. We construct the nerve complex $\mathcal{N}_\bullet(\mathcal{P})$ to capture multi-way adjacency relationships:

$$\mathcal{N}_p(\mathcal{P}) = \{S \subset \mathcal{P} : |S| = p + 1 \text{ and } \bigcap_{C \in S} \overline{C} \neq \emptyset\}$$

where \overline{C} denotes the closure of cell C . The sequence

$$\mathcal{N}_\bullet(\mathcal{P}) = (\mathcal{N}_0(\mathcal{P}), \mathcal{N}_1(\mathcal{P}), \mathcal{N}_2(\mathcal{P}), \dots)$$

forms a simplicial complex. This simplicial complex constructed from the partition is called the nerve complex, and the construction that produces it is known as the nerve construction [12, 46, 70].

This construction generalizes beyond partitions. A covering of a space X is a collection of sets $\mathcal{U} = \{U_\alpha\}_{\alpha \in A}$ such that $X = \bigcup_{\alpha \in A} U_\alpha$. Unlike partitions, coverings allow arbitrarily complex overlaps between sets. Given any covering \mathcal{U} , we can form the nerve complex $\mathcal{N}_\bullet(\mathcal{U})$ by including a k -simplex whenever $k + 1$ sets from the covering have nonempty intersection. The partition case is simply a special instance where the sets have disjoint interiors.

In the case of a Voronoi tessellation with cells in general position, the nerve complex coincides precisely with the Delaunay triangulation [24, 5], providing a geometric realization of this abstract combinatorial structure. The nerve complex thus serves as a geometric descriptor that reveals structural properties of the partition amenable to analysis and regularization. The partition itself, with its potentially complex local prediction functions, remains the primary object.

The construction yields different structures for different partition types encountered in machine learning. For axis-aligned decision trees in \mathbb{R}^n , the hyperrectangular cells meet along $(n - 1)$ -dimensional facets, $(n - 2)$ -dimensional edges, and so forth, down to vertices where 2^n cells meet. Each such vertex contributes a $(2^n - 1)$ -simplex to the nerve complex, making these complexes $(2^n - 1)$ -dimensional. MARS models [31] create similar hyperrectangular partitions but with a crucial difference that the cell maps f_α are continuous along cell boundaries (not affecting the geometric structure of the nerve complex). On the other hand, the dimension of the Delaunay complex associated with a Voronoi tessellation of an n -dimensional region of \mathbb{R}^n is always n . Oblique decision trees [50] and other methods using general hyperplane splits create convex polyhedral cells that can meet in various configurations. While axis-aligned splits necessarily create vertices where 2^n cells meet, oblique splits allow more flexibility. In general position, n hyperplanes through a point still create 2^n regions, but the specific configuration of splits in a trained model may result in fewer cells meeting at any given point, potentially yielding nerve complexes of lower dimension. The dimension of the resulting simplicial complex reflects both the ambient dimension and the specific geometric configuration of the partition.

2.2.2 Riemannian Structure on Partition Simplicial Complexes

When three cells meet at a point, what distinguishes a balanced configuration from a pathological one? The simplicial complex captures which cells are adjacent, but this combinatorial information alone cannot distinguish between fundamentally different geometric configurations. Consider three cells meeting at a point. In one configuration, they meet symmetrically with 120-degree angles between their boundaries, suggesting a balanced partition. In another, two cells form a narrow wedge against the third, creating sharp angles

that may indicate overfitting or poor generalization. A graph representation treating these configurations identically would miss this crucial geometric distinction.

How can we capture these angular relationships? What about the relative sizes of shared boundaries? When cells meet at unusual angles or have vastly different volumes, these geometric features may signal problems with the partition structure. To detect and quantify such properties, we need to enrich our simplicial complex with geometric information.

Just as Riemannian metrics enrich smooth manifolds with notions of length, angle, and curvature, partition complexes can be equipped with a Riemannian structure. This additional structure assigns inner products to the spaces associated with each simplex, enabling us to measure angles between edges, volumes of cells, and areas of boundaries. These measurements transform the discrete complex into a computational framework where geometric properties become accessible for analysis and regularization.

From Smooth to Discrete Riemannian Geometry To understand how geometric concepts translate from smooth manifolds to simplicial complexes, we begin with familiar ideas from linear algebra. In Euclidean space \mathbb{R}^n , the standard inner product $\langle v, w \rangle = v^T w$ enables us to compute lengths $\|v\| = \sqrt{\langle v, v \rangle}$ and angles $\cos(\theta) = \langle v, w \rangle / (\|v\| \|w\|)$. Any positive definite matrix A defines an alternative inner product $\langle v, w \rangle_A = v^T A w$, inducing a different geometry where lengths and angles are measured differently.

A smooth manifold like the unit sphere S^2 in \mathbb{R}^3 inherits geometric structure from the ambient space. At each point $x \in S^2$, there exists a tangent space $T_x S^2$ consisting of all vectors tangent to the sphere at x . The Euclidean inner product of \mathbb{R}^3 restricts to an inner product on each tangent space. While each individual tangent space just has the standard inner product, the crucial point is that these tangent spaces themselves are rotating as we move around the sphere. This variation of the tangent spaces from point to point is what creates curvature.

To see this concretely: if you parallel transport a vector around a closed loop on S^2 , it returns rotated relative to its starting position. This rotation is a manifestation of curvature, even though at each point we're using the "standard" inner product on that tangent space. The Riemannian metric encodes not just the inner products, but implicitly the entire geometric relationship between nearby tangent spaces.

The key insight is that simplicial complexes possess an analogous, though discrete, structure. While a point on a smooth manifold has infinitesimally small neighborhoods, a vertex v in a simplicial complex K has a discrete neighborhood: its star $\text{Star}(v) = \{\sigma \in K : v \in \sigma\}$, consisting of all simplices containing v . The edges emanating from v play the role of "discrete tangent vectors," and the space of formal linear combinations of these edges, denoted $\Lambda_1(\text{Star}(v))$, serves as the discrete analogue of a tangent space.

This correspondence extends systematically. The exterior powers $\Lambda^p T_x M$ of tangent spaces, which encode p -dimensional infinitesimal volumes, correspond to spaces $\Lambda_p(\text{Star}(v))$ of p -chains in the star. Similarly, differential forms on manifolds, which are integrated over submanifolds, correspond to cochains on simplicial complexes, which are evaluated on chains.

Building the Discrete Riemannian Structure We now formalize these ideas. For a simplicial complex K , the space of oriented p -chains supported on a subcomplex $L \subseteq K$ is:

$$\Lambda_p(L) = \left\{ \sum_{\sigma \in L_p} a_\sigma \cdot v_{i_0} \wedge v_{i_1} \wedge \cdots \wedge v_{i_p} : a_\sigma \in \mathbb{R} \right\} / \sim$$

where L_p denotes the set of p -simplices in L , each simplex $\sigma = \{v_{i_0}, v_{i_1}, \dots, v_{i_p}\}$ is represented by the formal wedge product $v_{i_0} \wedge v_{i_1} \wedge \cdots \wedge v_{i_p}$, and \sim is the equivalence relation

$$v_{\pi(0)} \wedge v_{\pi(1)} \wedge \cdots \wedge v_{\pi(p)} \sim \text{sgn}(\pi) \cdot v_0 \wedge v_1 \wedge \cdots \wedge v_p$$

for any permutation π . This antisymmetry relation ensures that the wedge product encodes orientation: even permutations preserve the orientation while odd permutations reverse it. Our notation $\Lambda_p(L)$, rather than the classical $C_p(L)$, emphasizes that simplices are treated as antisymmetric tensors, reflecting the deep connection between oriented simplicial chains and exterior algebra.

Having established the chain spaces $\Lambda_p(L)$ for subcomplexes of K , we can now formalize the Riemannian structure that encodes geometric information throughout the complex. A Riemannian simplicial complex consists of a simplicial complex K equipped with a compatible family of inner products

$$\langle \cdot, \cdot \rangle_{\sigma,p} : \Lambda_p(\overline{\text{Star}}(\sigma)) \times \Lambda_p(\overline{\text{Star}}(\sigma)) \rightarrow \mathbb{R}$$

defined for all simplices $\sigma \in K$ and all dimensions $p \geq 0$, where $\overline{\text{Star}}(\sigma)$ denotes the closed star of σ (the smallest subcomplex containing all simplices that have σ as a face).

The compatibility of these inner products is ensured through two fundamental conditions. First, the consistency condition requires that when a p -chain τ belongs to multiple star complexes, its self-inner product remains invariant:

$$\langle \tau, \tau \rangle_{\sigma,p} = \langle \tau, \tau \rangle_{\sigma',p}$$

for all $\tau \in \overline{\text{Star}}(\sigma) \cap \overline{\text{Star}}(\sigma')$. This ensures that geometric quantities such as lengths and volumes are well-defined regardless of the local context in which they are computed.

Second, the restriction compatibility addresses the hierarchical nature of simplicial complexes. When $\tau \subseteq \sigma$, the containment $\overline{\text{Star}}(\sigma) \subseteq \overline{\text{Star}}(\tau)$ induces a natural restriction map

$$r_{\sigma,\tau} : \Lambda_p(\overline{\text{Star}}(\tau)) \rightarrow \Lambda_p(\overline{\text{Star}}(\sigma))$$

For chains $\rho, \rho' \in \Lambda_p(\overline{\text{Star}}(\sigma))$, the compatibility requires

$$\langle \rho, \rho' \rangle_{\sigma,p} = \langle \rho, \rho' \rangle_{\tau,p}.$$

This condition ensures that geometric measurements respect the inclusion relationships between simplices, allowing local geometric information to assemble consistently into a global structure. The compatibility conditions reveal that for each $p \geq 0$, the collection of chain spaces $\{\Lambda_p(\overline{\text{Star}}(\sigma))\}_{\sigma \in K}$ forms a sheaf over K , with restriction maps satisfying the sheaf axioms [15, 42].

These compatibility conditions provide more than technical coherence; they encode a fundamental principle of geometric consistency. Just as a Riemannian manifold requires that tangent space inner products vary smoothly, a Riemannian simplicial complex requires that star complex inner products fit together compatibly. This compatibility enables the passage from local geometric data to global geometric invariants, a theme that pervades our subsequent constructions.

The relationship to weighted graphs illuminates the generality of this framework. A one-dimensional simplicial complex, consisting only of vertices and edges, equipped with a Riemannian structure, extends the notion of a weighted graph. At each vertex v , the inner product on $\Lambda_0(\overline{\text{Star}}(v)) = \text{span}\{v\}$ assigns a vertex weight. The inner product on $\Lambda_1(\overline{\text{Star}}(v))$ provides richer information than simple edge weights: it defines a Gram matrix whose diagonal entries determine edge weights and whose off-diagonal entries encode angular relationships between edges meeting at v . For an edge $e = v \wedge w$, the consistency condition ensures $\langle e, e \rangle_{v,1} = \langle e, e \rangle_{w,1}$, yielding a unique edge weight $w_e = \langle e, e \rangle_{v,1}^{1/2}$. However, for two edges $e_1 = v \wedge w_1$ and $e_2 = v \wedge w_2$ meeting at v , the inner product $\langle e_1, e_2 \rangle_{v,1}$ captures their geometric relationship at v , information absent in classical weighted graphs. This additional structure becomes essential when modeling systems where angular relationships matter, such as molecular conformations or mesh geometries.

The passage from smooth to discrete is justified by deep results in differential topology. Every smooth manifold admits triangulations that approximate its geometry arbitrarily well [71, 49], and the discrete operators converge to their smooth counterparts under refinement [38, 25]. This convergence theory validates our use of simplicial complexes for analyzing partition models while providing concrete computational tools.

Central to this correspondence is the preservation of fundamental calculus structures in the discrete setting. Just as smooth manifolds support differential forms and the exterior derivative, simplicial complexes support cochains and coboundary operators [13, 69]. The boundary operator

$$\partial_p : \Lambda_p(K) \rightarrow \Lambda_{p-1}(K)$$

generalizes the notion of taking boundaries:

$$\partial_p(v_0 \wedge \cdots \wedge v_p) = \sum_{j=0}^p (-1)^j v_0 \wedge \cdots \wedge \hat{v}_j \wedge \cdots \wedge v_p$$

where \hat{v}_j indicates omission of vertex v_j . Its dual, the coboundary operator

$$\delta_p : \Omega^p(K) \rightarrow \Omega^{p+1}(K)$$

on cochains (discrete differential forms), is defined by

$$(\delta_p \omega)(\sigma) = \omega(\partial_{p+1} \sigma).$$

This definition ensures that the discrete Stokes' theorem holds:

$$\langle \delta_p \omega, \sigma \rangle = \langle \omega, \partial_{p+1} \sigma \rangle$$

where $\langle \cdot, \cdot \rangle$ denotes the pairing between cochains and chains.

The profound connection to smooth differential geometry emerges through integration. Under the de Rham map that sends a smooth differential form α to the cochain $\sigma \mapsto \int_\sigma \alpha$, the smooth exterior derivative d corresponds to the discrete coboundary δ . The defining property of δ then becomes a consequence of the classical Stokes' theorem:

$$\int_\sigma d\alpha = \int_{\partial\sigma} \alpha$$

This correspondence ensures our discrete framework maintains the essential structure of calculus, with the algebraic relation $\delta \circ \delta = 0$ reflecting the geometric fact that $d \circ d = 0$.

This preservation of Stokes' theorem is not merely a formal nicety, it ensures that our discrete geometric constructions respect conservation laws and variational principles that govern physical systems. When we construct discrete harmonic extensions and smoothing operators on simplicial complexes in Section 2.3, this foundational correspondence guarantees that our methods inherit the stability and convergence properties of their smooth counterparts. Moreover, this framework provides the foundation for richer geometric analyses, including discrete gradient flows and Morse-Smale complexes, that reveal additional structure in machine learning models.

Geometric Structure of Partition Complexes With this formal framework established, we can now specify the Riemannian structure for partition-induced simplicial complexes. For partition-induced complexes, the Riemannian structure encodes the geometry of cell boundaries and their configurations. We begin by defining inner products on 0-chains (vertices). For a vertex v_i corresponding to cell C_i :

$$\langle v_i, v_i \rangle_{v_i,0} = \text{vol}_n(C_i)$$

This choice reflects that larger cells carry more "weight" in the geometric structure, analogous to mass distributions in physics.

For 1-chains, the fundamental building blocks are inner products between edges meeting at vertices. For edges $e = v_i \wedge v_j$ and $e' = v_i \wedge v_k$ in $\overline{\text{Star}}(v_i)$, representing cells C_i, C_j, C_k with C_i adjacent to both C_j and C_k , we consider the boundaries $F_{ij} = \overline{C_i} \cap \overline{C_j}$ and $F_{ik} = \overline{C_i} \cap \overline{C_k}$.

When these boundaries are $(n - 1)$ -dimensional (proper facets), we define:

$$\langle e, e' \rangle_{v_i,1} = \sqrt{\text{vol}_{n-1}(F_{ij}) \cdot \text{vol}_{n-1}(F_{ik})} \cdot \cos \theta_{jk} \quad (1)$$

where θ_{jk} is the interior dihedral angle of cell C_i between the hyperplanes H_{ij} and H_{ik} containing facets F_{ij} and F_{ik} .

To compute this angle in practice, we use the formula:

$$\cos \theta_{jk} = \frac{\mathbf{n}_{ij} \cdot \mathbf{n}_{ik}}{|\mathbf{n}_{ij}| |\mathbf{n}_{ik}|}$$

where \mathbf{n}_{ij} is the normal vector to H_{ij} pointing into C_i and \mathbf{n}_{ik} is the normal vector to H_{ik} pointing away from C_i .

This convention arises from the following geometric observation: The interior angle is the length of the arc on the unit circle (in the plane perpendicular to both hyperplanes) that lies within cell C_i . When we parallel transport the inward-pointing normal \mathbf{n}_{ij} along this interior arc, we arrive at the outward-pointing normal \mathbf{n}_{ik} . Therefore, the angle between these specifically oriented normals equals the interior dihedral angle.

When the boundaries have dimension less than $n - 1$, we adopt the convention that the inner product is zero, reflecting that the cells do not share proper facets at vertex v_i .

The formula (1) captures both metric information (facet areas) and angular relationships (dihedral angles). The angle term $\cos \theta_{jk}$ quantifies the relative orientation of adjacent cells: perpendicular boundaries yield zero inner product, while aligned boundaries produce large values.

For the important case of hyperrectangular partitions arising from tree-based models and MARS, all boundaries are aligned with coordinate axes. Consequently, any two distinct boundaries meet at right angles, giving $\cos \theta_{jk} = 0$ for all $j \neq k$. This means the Gram matrices for such partitions are diagonal, with diagonal entries determined solely by boundary volumes. This geometric signature, zero off-diagonal entries, is characteristic of axis-aligned partition methods and simplifies many computations.

We use the geometric mean $\sqrt{\text{vol}_{n-1}(F_{ij}) \cdot \text{vol}_{n-1}(F_{ik})}$ to combine boundary volumes, which maintains homogeneity under scaling. Alternative choices, such as arithmetic or harmonic means, would lead to different geometric weightings and potentially different regularization properties.

This construction generalizes naturally to higher dimensions through Gram determinants. For a simplex $\sigma \in K$ and oriented edges $e = \sigma \wedge v$ and $e' = \sigma \wedge v'$ in $\Lambda_{\dim(\sigma)+1}(\text{Star}(\sigma))$, we define:

$$\langle \sigma \wedge v, \sigma \wedge v' \rangle_{\sigma, \dim(\sigma)+1} = \text{vol}_{n-\dim(\sigma)-1}(F_e)^{1/2} \cdot \text{vol}_{n-\dim(\sigma)-1}(F_{e'})^{1/2} \cdot \cos \phi,$$

where

$$F_e = \bigcap \{C_\alpha : v_\alpha \in \{\text{vertices of } \sigma\} \cup \{v\}\}$$

and similarly for $F_{e'}$. The volume term $\text{vol}_{n-\dim(\sigma)-1}(F)$ denotes the $(n - \dim(\sigma) - 1)$ -dimensional Lebesgue measure of the face when this dimension is positive.

To understand the angle ϕ , note that

$$F_\sigma = \bigcap \{C_\alpha : v_\alpha \in \{\text{vertices of } \sigma\}\}$$

contains both $F_e = F_\sigma \cap C_v$ and $F_{e'} = F_\sigma \cap C_{v'}$, where C_v and $C_{v'}$ are the cells corresponding to vertices v and v' respectively.

Within the affine span H_σ of F_σ (which has dimension $n - \dim(\sigma)$), $H_e = \text{span}(F_e)$ and $H_{e'} = \text{span}(F_{e'})$ are hyperplanes of codimension 1 in H_σ . The interior dihedral angle ϕ between these hyperplanes is measured as the arc length on the unit circle in the plane perpendicular to both H_e and $H_{e'}$ within H_σ .

Following our convention for interior angles:

$$\cos \phi = \frac{\mathbf{n}_e \cdot \mathbf{n}_{e'}}{|\mathbf{n}_e| |\mathbf{n}_{e'}|}$$

where \mathbf{n}_e and $\mathbf{n}_{e'}$ are normal vectors to H_e and $H_{e'}$ within H_σ , with \mathbf{n}_e pointing toward C_v and $\mathbf{n}_{e'}$ pointing away from $C_{v'}$.

This construction naturally handles all possible dimensional configurations. When $\dim(\sigma) = 0$ (vertices), we recover the $(n-1)$ -dimensional facet intersections from our earlier edge construction. As $\dim(\sigma)$ increases, the dimension $n - \dim(\sigma) - 1$ of the intersection decreases accordingly, capturing the natural constraint that when more cells meet simultaneously, they do so in lower-dimensional manifolds. For instance, in \mathbb{R}^3 , two cells meet along 2D faces, three cells meet along 1D edges, and four cells meet at 0D points. The formula automatically adapts to measure volumes in the appropriate dimension for each configuration.

In the special case where $n - \dim(\sigma) - 1 = 0$, indicating point intersections, we adopt the convention that $\text{vol}_0(F) = 1$ if F is non-empty and $\text{vol}_0(F) = 0$ otherwise. For such zero-dimensional intersections, we set $\cos \phi = 1$ when both intersections are non-empty, reflecting the discrete nature of point intersections where angular measurements are not meaningful. This convention maintains consistency across dimensions while acknowledging the fundamental difference between continuous geometric measurements and discrete intersection patterns.

For p -simplices $\rho = \sigma \wedge v_1 \wedge \cdots \wedge v_q$ and $\rho' = \sigma \wedge v'_1 \wedge \cdots \wedge v'_q$ in $\Lambda_p(\overline{\text{Star}(\sigma)})$, where $q = p - \dim(\sigma)$, the inner product is defined as:

$$\langle \rho, \rho' \rangle_{\sigma, p} = \det(G_{\rho, \rho'})$$

where the Gram matrix has entries

$$[G_{\rho, \rho'}]_{ij} = \langle \sigma \wedge v_i, \sigma \wedge v'_j \rangle_{\sigma, \dim(\sigma)+1}.$$

This determinant formula, standard in multilinear algebra, extends the notion of volume from Euclidean space to our discrete setting. This construction represents the unique extension of inner products from edges to higher-dimensional simplices that respects the multilinear structure of exterior powers. The determinant formula ensures that the inner product on pp p -chains is induced from the inner products on edges through the natural algebraic structure, preserving orientation and capturing pp p -dimensional volumes [30, 72].

Example: Three Cells Meeting at a Vertex We can now make precise the geometric distinctions raised at the beginning of this section. Consider three cells C_1, C_2, C_3 meeting at a vertex v in \mathbb{R}^2 . The three edges at v are: $e_1 = v \wedge v_1$, $e_2 = v \wedge v_2$, and $e_3 = v \wedge v_3$. For the 2-simplex $\rho = v \wedge v_1 \wedge v_2$, the Gram matrix is:

$$G_\rho = \begin{pmatrix} \langle e_1, e_1 \rangle_v & \langle e_1, e_2 \rangle_v \\ \langle e_2, e_1 \rangle_v & \langle e_2, e_2 \rangle_v \end{pmatrix} = \begin{pmatrix} \text{vol}_{n-1}(F_{v, v_1}) & \gamma_{12} \\ \gamma_{12} & \text{vol}_{n-1}(F_{v, v_2}) \end{pmatrix}$$

where $\gamma_{12} = \sqrt{\text{vol}_{n-1}(F_{v, v_1}) \cdot \text{vol}_{n-1}(F_{v, v_2})} \cos \theta_{12}$. The determinant captures both the areas of boundaries and their angular relationship. For axis-aligned partitions where $\theta_{12} = 90$, the off-diagonal terms vanish, yielding

$$\det(G_\rho) = \text{vol}_{n-1}(F_{v, v_1}) \cdot \text{vol}_{n-1}(F_{v, v_2}),$$

a simple product of boundary lengths.

Example: Riemannian Structure on Tree Partitions Consider a decision tree in \mathbb{R}^2 creating four cells through perpendicular splits at $x_1 = 2$ and $x_2 = 1$ (for $x_1 < 2$) and $x_2 = 3$ (for $x_1 \geq 2$).

For the 0-chain structure, if the domain is $[0, 4] \times [0, 4]$, then:

- $\langle v_1, v_1 \rangle_{v_1,0} = \text{vol}_2(C_1) = 2 \times 1 = 2$
- $\langle v_2, v_2 \rangle_{v_2,0} = \text{vol}_2(C_2) = 2 \times 3 = 6$
- $\langle v_3, v_3 \rangle_{v_3,0} = \text{vol}_2(C_3) = 2 \times 1 = 2$
- $\langle v_4, v_4 \rangle_{v_4,0} = \text{vol}_2(C_4) = 2 \times 3 = 6$

For the 1-chain structure at vertex v_1 representing cell $C_1 = \{x_1 < 2, x_2 < 1\}$:

- The boundary F_{12} with cell $C_2 = \{x_1 < 2, x_2 \geq 1\}$ is the line segment $\{(x_1, 1) : x_1 < 2\}$ with length 2.
- The boundary F_{13} with cell $C_3 = \{x_1 \geq 2, x_2 < 1\}$ is the line segment $\{(2, x_2) : x_2 < 1\}$ with length 1.

These boundaries meet at right angles at point $(2, 1)$, so $\cos \theta_{23} = 0$. The Gram matrix at v_1 becomes:

$$G_{v_1} = \begin{pmatrix} \langle e_{12}, e_{12} \rangle_{v_1,1} & \langle e_{12}, e_{13} \rangle_{v_1,1} \\ \langle e_{13}, e_{12} \rangle_{v_1,1} & \langle e_{13}, e_{13} \rangle_{v_1,1} \end{pmatrix} = \begin{pmatrix} 2 & 0 \\ 0 & 1 \end{pmatrix}$$

The condition number $\kappa(G_{v_1}) = 2$ indicates mild anisotropy in the partition structure at this vertex. The zero off-diagonal entries throughout the complex reflect the perpendicular nature of axis-aligned splits, a geometric signature of standard decision trees. For such axis-aligned partitions, condition numbers directly measure the ratios of boundary lengths (in 2D) or areas (in 3D), providing a clear geometric interpretation of partition regularity.

2.2.3 Ensemble Geometric Structures

When multiple decision trees partition the same feature space, how should we reconcile their different geometric views? Consider two trees in a random forest that split the same region differently. One tree might place a boundary through the middle of a cluster, while another respects the cluster's natural boundary. Some cells appear in nearly every tree, suggesting stable geometric structures, while others appear rarely, indicating disagreement about the appropriate partition.

This variation across trees contains valuable information. Regions where trees consistently agree likely represent robust patterns in the data, while regions of disagreement may indicate uncertainty or complexity. By tracking how often cells from different trees coincide or share boundaries, we can build a richer geometric picture than any single tree provides.

Tree ensembles $\mathcal{E} = \{T_1, T_2, \dots, T_B\}$ create multiple overlapping partitions of the feature space. Each tree T_b induces its own partition \mathcal{P}_{T_b} . The refined partition approach overlays all individual tree partitions:

$$\mathcal{P}_{\mathcal{E}} = \left\{ \bigcap_{b=1}^B C_{b,\alpha_b} : C_{b,\alpha_b} \in \mathcal{P}_{T_b} \right\} \setminus \{\emptyset\}$$

We now construct a Riemannian structure that captures both the geometry of this refined partition and the agreement patterns between trees in the ensemble.

The 0-chain structure. We begin with the simplest case: inner products on vertices. Each vertex v_i in the nerve complex corresponds to a cell C_i in the refined partition. Following our principle that cell volume reflects importance, we define:

$$\langle v_i, v_i \rangle_{v_i,0}^{\text{ens}} = \text{vol}_n(C_i) + \lambda_0 \cdot \text{Freq}(C_i)$$

where

$$\text{Freq}(C_i) = \frac{1}{B} \sum_{b=1}^B \mathbf{1}[C_i \subseteq \text{some cell of tree } b]$$

measures how many trees contribute to defining this cell.

The 1-chain structure. For edges, we must capture how the ensemble views adjacency relationships. Following the kernel perspective on random forests, we define the co-occurrence frequency between two cells:

$$K(C_i, C_j) = \frac{1}{B} \sum_{b=1}^B \mathbf{1}[\text{cells } C_{b,\alpha_b^{(i)}} \text{ and } C_{b,\alpha_b^{(j)}} \text{ are adjacent in tree } b]$$

This quantity, ranging from 0 to 1, measures how consistently the ensemble treats these cells as neighbors.

To create a Riemannian structure that captures both the refined partition's geometry and the ensemble's confidence in that geometry, we enhance the standard geometric inner products with ensemble-based terms. The geometric term captures the physical configuration (boundary sizes and angles), while the ensemble term adds information about statistical stability across the ensemble. We combine them additively so that edges can have non-zero inner product even when they meet at right angles (where the geometric term vanishes), allowing the ensemble agreement to maintain connectivity in the Riemannian structure. The ensemble term takes a similar functional form to the geometric term to ensure comparable scaling.

For edges $e = v_i \wedge v_j$ and $e' = v_i \wedge v_k$ in $\overline{\text{Star}}(v_i)$, we combine geometric information with ensemble agreement:

$$\langle e, e' \rangle_{v_i,1}^{\text{ens}} = \sqrt{\text{vol}_{n-1}(F_{ij}) \cdot \text{vol}_{n-1}(F_{ik}) \cdot \cos \theta_{jk}} + \lambda_1 \sqrt{K(C_i, C_j) \cdot K(C_i, C_k)}$$

where $F_{ij} = \overline{C_i} \cap \overline{C_j}$ and $\lambda_1 > 0$ weights the ensemble term.

For axis-aligned tree partitions, $\cos \theta_{jk} = 0$ for $j \neq k$, yielding:

$$\langle e, e' \rangle_{v_i,1}^{\text{ens}} = \begin{cases} \text{vol}_{n-1}(F_{ij}) + \lambda_1 K(C_i, C_j) & \text{if } e = e' \\ \lambda_1 \sqrt{K(C_i, C_j) \cdot K(C_i, C_k)} & \text{if } e \neq e' \end{cases}$$

The off-diagonal terms, arising purely from ensemble agreement, quantify how similarly the trees view different adjacency relationships.

The general p-chain structure. The construction extends naturally to higher dimensions. For a collection of cells $\{C_{i_1}, C_{i_2}, \dots, C_{i_{p+1}}\}$, we generalize the co-occurrence frequency:

$$K(C_{i_1}, \dots, C_{i_{p+1}}) = \frac{1}{B} \sum_{b=1}^B \mathbf{1}[\text{cells } C_{b, \alpha_b^{(i_1)}}, \dots, C_{b, \alpha_b^{(i_{p+1})}} \text{ form a } p\text{-simplex in tree } b]$$

This measures how often these $p + 1$ cells simultaneously meet in individual trees.

For p -simplices $\rho = \sigma \wedge v_1 \wedge \dots \wedge v_q$ and $\rho' = \sigma \wedge v'_1 \wedge \dots \wedge v'_q$ in $\Lambda_p(\overline{\text{Star}(\sigma)})$, we define:

$$\langle \rho, \rho' \rangle_{\sigma, p}^{\text{ens}} = \langle \rho, \rho' \rangle_{\sigma, p}^{\text{geom}} + \lambda_p \cdot K_p(\rho, \rho')$$

where the geometric term follows Section 2.2.2, and the ensemble term uses:

$$K_p(\rho, \rho') = \det(K_{\rho, \rho'})$$

The Gram matrix $K_{\rho, \rho'}$ has entries:

$$[K_{\rho, \rho'}]_{ij} = K(\text{vertices of } \sigma \cup \{v_i\}, \text{vertices of } \sigma \cup \{v'_j\})$$

More explicitly, if σ has vertices $\{u_1, \dots, u_k\}$, then:

$$[K_{\rho, \rho'}]_{ij} = K(u_1, \dots, u_k, v_i, u_1, \dots, u_k, v'_j)$$

For example, if $\sigma = v_0$ (a vertex), $\rho = v_0 \wedge v_1 \wedge v_2$ and $\rho' = v_0 \wedge v_3 \wedge v_4$, then:

$$K_{\rho, \rho'} = \begin{pmatrix} K(v_0, v_1, v_3) & K(v_0, v_1, v_4) \\ K(v_0, v_2, v_3) & K(v_0, v_2, v_4) \end{pmatrix}$$

Each entry measures how often the corresponding triple of cells forms a 2-simplex across the ensemble.

Choice of parameters. The weights λ_p balance geometric and ensemble contributions at each dimension. A natural choice ensures both terms have comparable scales:

$$\lambda_p = \bar{v}_p = \frac{1}{|K_p|} \sum_{\sigma \in K_p} \text{vol}_{n-p}(F_\sigma)$$

where $|K_p|$ denotes the number of p -simplices and F_σ is the face corresponding to simplex σ .

This construction reveals how ensemble methods naturally incorporate uncertainty into their geometric structure. High co-occurrence frequencies indicate stable geometric relationships that persist across the ensemble, while low frequencies identify regions where trees disagree about local structure. The Riemannian framework transforms these agreement patterns into geometric quantities that can guide refinement and regularization.

2.2.4 Gradient Boosting as Geometric Flow

What happens to the geometry of partitions as gradient boosting sequentially adds trees? Unlike random forests where all trees exist simultaneously, gradient boosting builds models incrementally, with each new tree modifying the ensemble's partition structure. Early trees might create broad regions capturing global patterns, while later trees add fine-grained cells to correct local errors. This sequential refinement suggests a dynamic process, but can we characterize it mathematically as a geometric flow?

Understanding this evolution could unlock new insights into gradient boosting's effectiveness and limitations. Does the partition geometry stabilize as training progresses, or does it become increasingly fragmented? When should we stop adding trees based on geometric rather than purely predictive criteria? By viewing gradient boosting through the lens of evolving geometric structures, we can develop principled approaches to model selection and regularization that go beyond monitoring training error.

Gradient boosting exhibits a natural geometric interpretation when viewed through the lens of evolving Riemannian structures. Unlike random forests where all trees contribute simultaneously, gradient boosting sequentially adds trees, creating a dynamic evolution of the partition geometry. At iteration m , the ensemble consists of trees T_1, T_2, \dots, T_m with the refined partition:

$$\mathcal{P}^{(m)} = \left\{ \bigcap_{i=1}^m C_{i,k_i} : C_{i,k_i} \in \mathcal{P}_{T_i} \right\} \setminus \{\emptyset\}$$

As we add trees, both the partition structure and the co-occurrence frequencies evolve. Each cell in the refined partition at iteration m has the form $C_i^{(m)} = \bigcap_{b=1}^m C_{b,\alpha_b^{(i)}}$ where $C_{b,\alpha_b^{(i)}} \in \mathcal{P}_{T_b}$ is the cell from tree b that participates in forming $C_i^{(m)}$.

The co-occurrence frequency at iteration m for cells $C_i^{(m)}$ and $C_j^{(m)}$ is:

$$K^{(m)}(C_i^{(m)}, C_j^{(m)}) = \frac{1}{m} \sum_{b=1}^m \mathbf{1}[\text{cells } C_{b,\alpha_b^{(i)}} \text{ and } C_{b,\alpha_b^{(j)}} \text{ are adjacent in tree } b]$$

When tree T_{m+1} is added, the refined partition may change. A cell $C_i^{(m)}$ may be split into multiple cells in $\mathcal{P}^{(m+1)}$, or it may remain intact if $C_{m+1,\alpha_{m+1}^{(i)}}$ (the corresponding cell in tree T_{m+1}) fully contains it. For cells $C_i^{(m+1)}$ and $C_j^{(m+1)}$ in the new refined partition:

$$K^{(m+1)}(C_i^{(m+1)}, C_j^{(m+1)}) = \frac{1}{m+1} \sum_{b=1}^{m+1} \mathbf{1}[\text{cells } C_{b,\alpha_b^{(i)}} \text{ and } C_{b,\alpha_b^{(j)}} \text{ are adjacent in tree } b]$$

For the Riemannian structure, following Section 2.2.3, edges $e = v_i \wedge v_j$ and $e' = v_i \wedge v_k$ have inner product:

$$\langle e, e' \rangle_{v_i,1}^{(m)} = \sqrt{\text{vol}_{n-1}(F_{ij}^{(m)}) \cdot \text{vol}_{n-1}(F_{ik}^{(m)})} \cdot \cos \theta_{jk} + \lambda_1 \sqrt{K^{(m)}(C_i^{(m)}, C_j^{(m)}) \cdot K^{(m)}(C_i^{(m)}, C_k^{(m)})}$$

For axis-aligned trees where $\cos \theta_{jk} = 0$ for $j \neq k$, this simplifies to:

$$\langle e, e' \rangle_{v_i, 1}^{(m)} = \begin{cases} \text{vol}_{n-1}(F_{ij}^{(m)}) + \lambda_1 K^{(m)}(C_i^{(m)}, C_j^{(m)}) & \text{if } e = e' \\ \lambda_1 \sqrt{K^{(m)}(C_i^{(m)}, C_j^{(m)}) \cdot K^{(m)}(C_i^{(m)}, C_k^{(m)})} & \text{if } e \neq e' \end{cases}$$

The evolution of the inner product structure reveals how boosting modifies geometry:

$$\langle e, e' \rangle_{v_i, 1}^{(m+1)} - \langle e, e' \rangle_{v_i, 1}^{(m)} = \Delta_{\text{geom}} + \Delta_{\text{ens}}$$

For the diagonal case ($e = e' = v_i \wedge v_j$):

$$\Delta_{\text{geom}} = \text{vol}_{n-1}(F_{ij}^{(m+1)}) - \text{vol}_{n-1}(F_{ij}^{(m)})$$

$$\Delta_{\text{ens}} = \lambda_1 \left[K^{(m+1)}(C_i^{(m)}, C_j^{(m)}) - K^{(m)}(C_i^{(m)}, C_j^{(m)}) \right] = \frac{\lambda_1}{m+1} \left[\mathbf{1}[\text{adjacent in } T_{m+1}] - K^{(m)}(C_i^{(m)}, C_j^{(m)}) \right]$$

For the off-diagonal case ($e = v_i \wedge v_j$, $e' = v_i \wedge v_k$ with $j \neq k$):

$$\Delta_{\text{geom}} = 0 \quad (\text{for axis-aligned trees})$$

$$\Delta_{\text{ens}} = \lambda_1 \left[\sqrt{K^{(m+1)}(C_i^{(m)}, C_j^{(m)}) \cdot K^{(m+1)}(C_i^{(m)}, C_k^{(m)})} - \sqrt{K^{(m)}(C_i^{(m)}, C_j^{(m)}) \cdot K^{(m)}(C_i^{(m)}, C_k^{(m)})} \right]$$

The geometric change Δ_{geom} is non-zero only when tree T_{m+1} splits one or both of the cells $C_i^{(m)}$, $C_j^{(m)}$, creating a new or modified boundary. The ensemble change Δ_{ens} always occurs and can be positive (strengthening the connection) or negative (weakening it) depending on whether the new tree agrees with the existing ensemble structure.

The gradient boosting process thus traces a path through the space of Riemannian simplicial complexes, with each tree refining both the combinatorial structure (through new cells) and the geometric structure (through modified co-occurrence patterns). This dual evolution provides rich information about the learning dynamics, suggesting that geometric properties could guide both tree construction and stopping criteria. We explore these regularization possibilities in detail in the next section.

2.2.5 Geometric Regularization

How can we translate geometric insights into practical regularization strategies that improve model performance? Traditional regularization penalizes the number of parameters or tree depth, but these indirect constraints fail to address the spatial pathologies we have identified. A model might satisfy depth constraints while creating cells with extreme volume disparities, where tiny regions overfit to individual points while vast empty spaces remain in adjacent cells. Another might generate boundaries meeting at knife-sharp angles that will likely misclassify nearby test points. We need regularization that directly targets these geometric problems.

What would ideal geometric regularization achieve? It should penalize extreme volume ratios between cells, encouraging balanced partitions. It should discourage sharp angles

where cells meet, promoting smoother decision boundaries. For ensemble methods, it should reward geometric consensus—configurations where multiple models agree on stable boundary locations. By incorporating these geometric criteria into model training, we can guide learning algorithms toward partitions that not only fit the data but also exhibit the spatial regularity associated with good generalization.

The Riemannian structure on partition complexes enables the formulation of geometric regularization terms that complement classical approaches from Section 2.1.2. Rather than penalizing only the number of cells or the smoothness of functions within them, we can now formulate regularization terms that directly target spatial pathologies.

A key insight for high-dimensional applications is that real data typically exhibits low intrinsic dimensionality despite residing in high-dimensional feature spaces. Rather than computing geometric properties in the full ambient space, implementations should leverage local dimensionality reduction within each partition cell. By projecting to subspaces that retain 95-99% of local variance, we can ensure that geometric computations remain both meaningful and tractable. For instance, data in \mathbb{R}^{1000} might have an intrinsic dimensionality of approximately 10, reducing boundary volume computations from intractable high-dimensional operations to manageable calculations in this lower-dimensional representation. This dimensionality reduction approach provides a practical adaptation of our geometric framework to the realities of high-dimensional data.

With the geometric framework in place, penalties can explicitly depend on spatial properties of the partition. Natural geometric quantities include cell volumes $\text{vol}_n(C_\alpha)$, surface areas of partition boundaries $\text{vol}_{n-1}(\partial C_\alpha \cap \partial C_\beta)$, and angles between adjacent cells at their boundaries. Such penalties encourage balanced partitions with regular cell shapes and smooth transitions between regions. For instance, a geometric regularization term takes the form

$$R_{\text{geom}} = \sum_{\alpha} \phi(\text{vol}_n(C_\alpha)) + \sum_{\langle \alpha, \beta \rangle} \psi(\text{vol}_{n-1}(\partial C_\alpha \cap \partial C_\beta), \theta_{\alpha\beta}),$$

where ϕ penalizes extreme volumes, ψ incorporates both boundary size and the angle $\theta_{\alpha\beta}$ between cells, and the second sum runs over adjacent cell pairs.

As we will demonstrate, the Riemannian structure on partition-induced simplicial complexes provides a principled framework for computing and incorporating these geometric properties into regularization schemes. The simplicial complex naturally encodes adjacency relationships, while the Riemannian metric captures local geometric information including angles and volumes. This geometric perspective not only suggests alternative regularization strategies but also provides tools for analyzing existing methods through their implicit geometric biases.

Geometric Quantities and Their Statistical Interpretation The Riemannian structure enables computation of several geometric quantities with direct statistical relevance. Cell volumes, encoded in the diagonal entries of Gram matrices, indicate the "influence region" of each local model. Extreme volume disparities may signal overfitting, where the model creates tiny cells to accommodate outliers or noise. The condition numbers of vertex Gram matrices $\kappa(G_v)$ measure local anisotropy, with large values indicating stretched or poorly shaped cells that may not generalize well to new data.

Boundary properties provide complementary information. The total surface area of a cell’s boundary, $\sum_{j \sim i} \text{vol}_{n-1}(F_{ij})$ where the sum runs over adjacent cells, quantifies the cell’s complexity. Cells with large surface-to-volume ratios may indicate excessive fragmentation of the feature space. Dihedral angles between adjacent cells, extracted from the off-diagonal entries of Gram matrices, reveal the smoothness of decision boundaries. Sharp angles (small $\cos \theta$) suggest abrupt transitions that may indicate overfitting to training data patterns.

Higher-order simplices capture multi-way interactions between cells. The volume of a p -simplex, computed as $\sqrt{\det(G_\sigma)}$ for the Gram matrix on $\Lambda_p(\overline{\text{Star}}(\sigma))$, measures the ”strength” of the $(p + 1)$ -way intersection. Large volumes for high-dimensional simplices indicate complex intersection patterns that may be difficult to interpret or may result from overfitting.

General Formulation of Geometric Penalties Building on these quantities, we propose geometric regularization terms that can be incorporated into the training objectives of partition models. A general geometric regularization term takes the form:

$$R_{\text{geom}}(\mathcal{P}) = \sum_{k=0}^{\dim(K)} \lambda_k \sum_{\sigma \in K_k} \psi_k(\sigma)$$

where ψ_k are penalty functions operating on k -simplices and $\lambda_k \geq 0$ are regularization strengths for each dimension.

For vertices (0-simplices), natural penalties include:

$$\psi_0(v_i) = \phi \left(\frac{\text{vol}_n(C_i)}{\text{vol}_n(\mathcal{D})/|K_0|} \right) + \gamma \log(\kappa(G_{v_i}))$$

where ϕ is a convex function penalizing deviations from the average cell volume (e.g., $\phi(t) = t + 1/t$ for $t > 0$), and the second term penalizes anisotropic local geometry. This encourages balanced partitions with well-conditioned cells.

For edges (1-simplices), we can penalize both boundary complexity and sharp angles:

$$\psi_1(v_i \wedge v_j) = \text{vol}_{n-1}(F_{ij})^\alpha \cdot h(\theta_{ij})$$

where $\alpha > 1$ penalizes large boundaries and h penalizes extreme angles, e.g.,

$$h(\theta) = (\pi/2 - |\theta - \pi/2|)^2$$

favors perpendicular boundaries. This encourages partitions with moderate boundary sizes and avoids both very sharp and very shallow angles.

For higher-dimensional simplices, penalties can target complex intersection patterns:

$$\psi_p(\sigma) = \left(\frac{\text{vol}_p(\sigma)}{\text{vol}_p^{\text{ref}}} \right)^\beta \cdot \mathbf{1}[p > p_0]$$

where $\text{vol}_p^{\text{ref}}$ is a reference volume scale, $\beta > 0$ controls the penalty strength, and p_0 is a threshold beyond which high-order intersections are discouraged. This limits the combinatorial complexity of the partition.

Implementation in Partition Models These penalties can be incorporated into specific partition models as follows. For decision trees, the splitting criterion becomes:

$$\text{Score}(s) = \text{ImpurityReduction}(s) - \eta \cdot \Delta R_{\text{geom}}(s)$$

where $\Delta R_{\text{geom}}(s)$ is the change in geometric penalty from split s . This can be computed efficiently by maintaining local geometric information during tree construction.

In MARS models, geometric penalties augment the forward stepwise procedure. When considering adding a new basis function, we evaluate both the reduction in residual sum of squares and the induced change in partition geometry. The geometric penalty can favor basis functions that create more regular partitions, potentially improving model interpretability and generalization.

For random forests and other ensemble methods, geometric regularization can guide both individual model training and ensemble aggregation. Individual trees can be regularized to avoid extreme geometries, while the ensemble combination weights can be adjusted to favor geometrically compatible partitions. The co-occurrence frequencies $K(C_i, C_j)$ provide a natural measure of geometric compatibility across trees.

Geometric Regularization for Gradient Boosting In gradient boosting, the sequential nature of gradient boosting offers unique regularization opportunities through the geometric flow perspective developed in Section 2.2.4. We propose three complementary approaches:

The geometric flow perspective suggests the following monitoring criterion. Define the geometric energy at iteration m as:

$$E^{(m)} = \sum_{v \in K_0^{(m)}} \log \kappa(G_v^{(m)})$$

where $G_v^{(m)}$ is the Gram matrix at vertex v using the current Riemannian structure. We hypothesize that this geometric energy measure could potentially track the evolution of partition regularity during boosting. The rate of energy change:

$$\frac{E^{(m+1)} - E^{(m)}}{E^{(m)}} > \epsilon$$

provides a candidate geometric early stopping criterion that warrants empirical investigation.

Regularized tree construction. When fitting tree T_{m+1} in gradient boosting with general loss function $\ell(y, \hat{y})$, incorporate geometric objectives:

$$T_{m+1} = \arg \min_T \{ \mathcal{L}_{\text{residual}}(T) + \gamma \cdot \mathcal{R}_{\text{geom}}(T | \mathcal{P}^{(m)}) \}$$

where

$$\mathcal{L}_{\text{residual}}(T) = \sum_{i=1}^N \ell(y_i, F^{(m)}(x_i) + \eta f_T(x_i)),$$

η is the learning rate and $f_T(x_i)$ the prediction of tree T at point x_i . The geometric regularizer favors trees that maintain high co-occurrence with existing structure:

$$\mathcal{R}_{\text{geom}}(T|\mathcal{P}^{(m)}) = - \sum_{(i,j) \in \text{adjacent pairs in } T} K^{(m)}(C_i \cap \text{leaf}_T, C_j \cap \text{leaf}_T)$$

This encourages new trees to respect boundaries where previous trees agree, reducing geometric complexity.

Weighted co-occurrence. In standard gradient boosting with learning rate η , predictions combine as $F^{(m)}(x) = \sum_{i=1}^m \eta f_{T_i}(x)$. This suggests using weighted co-occurrence frequencies in the Riemannian structure:

$$K_\eta^{(m)}(C_i^{(m)}, C_j^{(m)}) = \frac{\sum_{b=1}^m \eta^b \mathbf{1}[\text{cells } C_{b,\alpha_b^{(i)}} \text{ and } C_{b,\alpha_b^{(j)}} \text{ are adjacent in tree } b]}{\sum_{b=1}^m \eta^b}$$

For $\eta < 1$, later trees contribute less to the geometric structure, reflecting their role in fine-tuning rather than establishing primary boundaries.

Spectral monitoring. The evolving Riemannian structure induces a sequence of Hodge Laplacian operators $\{\Delta_p^{(m)}\}_{p=0}^{\dim K}$ on the nerve complex of partition $\mathcal{P}^{(m)}$. These operators encode geometric properties at multiple scales, providing rich information about the evolution of partition structure during boosting.

The graph Laplacian on vertices is:

$$\Delta_0^{(m)} = D^{(m)} - A^{(m)}$$

where $D^{(m)}$ is the diagonal degree matrix and $A^{(m)}$ is the weighted adjacency matrix with entries:

$$A_{ij}^{(m)} = \begin{cases} \text{vol}_{n-1}(F_{ij}^{(m)}) + \lambda_1 K^{(m)}(C_i^{(m)}, C_j^{(m)}) & \text{if } C_i^{(m)} \text{ and } C_j^{(m)} \text{ are adjacent} \\ 0 & \text{otherwise} \end{cases}$$

The eigenvalues $0 = \lambda_1^{(m)} \leq \lambda_2^{(m)} \leq \dots$ encode global connectivity. The spectral gap $\lambda_2^{(m)}$ measures how well-connected the partition is, with large gaps indicating strong connectivity and coherent geometric structure, while small gaps suggest near-disconnection through fragmentation or geometric bottlenecks.

Higher-order Hodge Laplacians $\Delta_p^{(m)} = \partial_{p+1} \partial_{p+1}^* + \partial_p^* \partial_p$ for $p \geq 1$ capture multi-way interactions beyond pairwise relationships. The edge Laplacian $\Delta_1^{(m)}$ reveals patterns in edge flows and boundary cycles, while $\Delta_2^{(m)}$ captures the structure of triple cell intersections in three or more dimensions. Higher-order Laplacians encode increasingly complex multi-way meeting patterns, providing a complete multi-scale view of the partition's geometric structure.

The complete spectral signature tracks geometric robustness across scales:

$$\text{SpectralSignature}^{(m)} = \left(\frac{\lambda_2^{(m)}}{\lambda_2^{(1)}}, \frac{\mu_{1,1}^{(m)}}{\mu_{1,1}^{(1)}}, \frac{\mu_{2,1}^{(m)}}{\mu_{2,1}^{(1)}}, \dots \right)$$

where $\mu_{p,1}^{(m)}$ is the smallest positive eigenvalue of $\Delta_p^{(m)}$.

Decreasing ratios suggest loss of geometric robustness at the corresponding scale. We propose monitoring:

$$\text{GeometricHealth}^{(m)} = \min_{p:\mu_{p,1}^{(1)}>0} \frac{\mu_{p,1}^{(m)}}{\mu_{p,1}^{(1)}}$$

When this measure drops below a threshold, it may indicate the ensemble is transitioning from learning robust structure to overfitting, though empirical validation is needed to establish appropriate thresholds for specific applications.

For computational efficiency, only the first few eigenvalues at each scale need be computed using iterative methods.

Comparison with Classical Regularization Classical machine learning regularization and geometric regularization fundamentally differ in their approach to controlling model complexity. Standard parameter regularization, such as L1 or L2 penalties on weight vectors, controls model capacity globally through constraints like $\|w\|_2^2$ but remains agnostic to the local geometric structure of the induced partition. Similarly, structural regularization approaches that limit tree depth or the number of parameters impose uniform complexity constraints without considering the quality or configuration of the resulting partition. In contrast, geometric regularization directly targets specific spatial pathologies such as cells with extreme volume disparities, boundaries meeting at sharp angles, or surface-area-to-volume ratios that indicate excessive fragmentation. While standard regularization may indirectly influence partition geometry through its constraints on model parameters, geometric regularization provides direct control over these spatial properties. This direct control over geometric structure offers the potential for models that not only generalize better but also exhibit more interpretable decision boundaries and more balanced spatial decompositions of the feature space.

These geometric regularization strategies apply the mathematical structures of Sections 2.2.1-2.2.4 to partition model training. By penalizing geometric irregularities directly, this approach addresses limitations of classical regularization approaches that focus solely on model complexity or function smoothness. The result is a principled framework for creating partition models with better generalization properties and more interpretable geometric structures.

2.3 Refinement of Partition Models

The geometric framework developed in Section 2.2 can be extended to address the refinement of piecewise constant predictions in partition models. A decision tree predicts 0.2 in one cell and 0.8 in an adjacent cell, creating an abrupt jump at their boundary. Should we accept this discontinuity, or is there information in the geometric structure that could guide smoothing? When three cells meet at a vertex with values 0.2, 0.8, and 0.5, how should their angular configuration influence interpolation?

This challenge reflects a fundamental limitation: while partition models produce piecewise constant predictions, they often approximate smooth phenomena. A tree modeling house prices creates sharp boundaries between neighborhoods, yet prices vary continuously across space. Standard graph-based smoothing methods address this by updating values using weighted averages along edges. However, these methods treat each edge independently. When three cells meet at a vertex, graph Laplacian smoothing cannot distinguish whether they meet symmetrically or form a narrow wedge, potentially smoothing inappropriately.

The importance of higher-order geometric relationships becomes clear in structured prediction tasks. In molecular property prediction, aromatic rings fundamentally alter chemical behavior through resonance effects that cannot be decomposed into pairwise bond properties. A model that smooths predictions based only on pairwise atomic connections would miss these collective effects, potentially leading to systematic errors for aromatic compounds. Similarly, in computer vision tasks on mesh data, the curvature at a vertex, determined by how surrounding triangles meet, often correlates strongly with semantic boundaries. These examples demonstrate that multi-way geometric relationships contain essential information that pairwise methods cannot capture.

This section develops refinement techniques that exploit the full geometric structure of partition models. We extend classical smoothing operators to respect not just adjacency but the complete simplicial geometry, incorporating information from triangles, tetrahedra, and higher-order structures. The key insight is that smoothing should respect not just which cells are adjacent, but how they meet in space.

We construct the extended Laplacian through a careful lifting procedure. Given a function u defined on vertices of our simplicial complex K , we must first extend it to higher-dimensional simplices before applying appropriate smoothness operators. The lifting process reveals a deep connection between discrete and continuous mathematics.

The Whitney form method provides an elegant approach to lifting vertex functions to higher-dimensional simplices. For each p -simplex $\sigma = [v_0, \dots, v_p]$, Whitney introduced a canonical p -form

$$\omega_\sigma = p! \sum_{i=0}^p (-1)^i \lambda_i d\lambda_0 \wedge \dots \wedge \widehat{d\lambda_i} \wedge \dots \wedge d\lambda_p$$

where $(\lambda_0, \dots, \lambda_p)$ are barycentric coordinates (satisfying $\sum_i \lambda_i = 1$ and $\lambda_i \geq 0$) and the hat denotes omission. This form has the remarkable property that

$$\int_\tau \omega_\sigma = \begin{cases} 1 & \text{if } \tau = \sigma \\ 0 & \text{if } \tau \neq \sigma \end{cases}$$

To lift a vertex function u to a p -cochain using Whitney forms, we evaluate:

$$\kappa_p^{\text{Whitney}}(u)(\sigma) = \sum_{i=0}^p u(v_i) \int_\sigma \lambda_i d\lambda_0 \wedge \dots \wedge \widehat{d\lambda_i} \wedge \dots \wedge d\lambda_p$$

This formula interpolates the vertex values $u(v_i)$ using integrals of the barycentric coordinates against the appropriate volume forms.

An alternative lifting approach uses harmonic extension, seeking the function on each simplex that minimizes the Dirichlet energy while matching prescribed vertex values. For each p -simplex σ , we solve Laplace's equation $\Delta H = 0$ with the vertex values of u as boundary conditions. Among all functions with these boundary values, the harmonic function has the smallest integrated squared gradient $\int_{\sigma} \|\nabla H\|^2$, making it "smoothest" in this specific energy-minimizing sense.

Remarkably, both the Whitney extension and harmonic extension yield the same result: the lifted value on a p -simplex σ is the barycentric average of the vertex values, weighted by the p -dimensional volume of the simplex:

$$\kappa_p(u)(\sigma) = \frac{\text{vol}_p(\sigma)}{p+1} \sum_{i=0}^p u(v_i)$$

This formula shows that higher-dimensional simplices naturally encode averaged information from their vertices (see Appendix A for the complete derivation).

With lifting operators in hand, we can now define the extended Laplacian. Let L_p denote the Hodge Laplacian acting on p -cochains, defined through

$$L_p = \delta_{p-1} \delta_{p-1}^* + \delta_p^* \delta_p$$

where δ is the coboundary operator.

The extended Laplacian combines information from different dimensions:

$$L_{\text{ext}} u = \underbrace{L_0 u}_{\text{pairwise smoothing}} + \underbrace{\alpha_1 \kappa_1^* L_1 \kappa_1 u}_{\text{loop consistency}} + \underbrace{\alpha_2 \kappa_2^* L_2 \kappa_2 u}_{\text{triple interactions}} + \dots$$

Each term enforces smoothness at a different scale:

- $L_0 u$: Standard graph Laplacian smoothing along edges
- $\kappa_1^* L_1 \kappa_1 u$: Ensures gradients are consistent around loops
- $\kappa_2^* L_2 \kappa_2 u$: Regularizes curvature-like quantities

In general, the term $\kappa_p^* L_p \kappa_p$ incorporates p -dimensional smoothness information. The operator κ_p lifts vertex functions to p -cochains using the Whitney/harmonic method, L_p measures roughness in that dimension, and κ_p^* projects back to vertices. The parameters $\alpha_p > 0$ control the relative influence of each dimension.

The extended Laplacian addresses the motivating problem by incorporating multi-way cell interactions. When three cells meet at unusual angles, the 2-dimensional term $\kappa_2^* L_2 \kappa_2$ detects this through the geometry encoded in the triangle they form. The resulting smoothing respects not just adjacency but the full configuration of how cells meet.

A complementary variational approach emerges through simplicial splines. Given observations $y = (y_1, \dots, y_n)^T$ at vertices, we seek a function minimizing the energy functional:

$$\mathcal{E}[u] = \underbrace{\|y - u\|^2}_{\text{data fidelity}} + \underbrace{\sum_{p=0}^d \sum_{k=1}^{K_p} \lambda_{pk} \langle \kappa_p u, L_p^k \kappa_p u \rangle_p}_{\text{multi-scale regularization}}$$

This functional balances fidelity to observed data against smoothness constraints operating at multiple geometric scales. The regularization term decomposes into contributions from different dimensions, each capturing distinct aspects of smoothness. At the lowest dimension ($p = 0$), the penalty directly constrains differences between vertex values, encouraging nearby vertices to have similar function values. The one-dimensional component ($p = 1$) penalizes variation along edges, analogous to controlling first derivatives in the continuous setting. This term ensures that the discrete gradient field varies smoothly throughout the complex.

Higher-dimensional terms encode increasingly sophisticated notions of regularity. The two-dimensional component ($p = 2$) measures variation across triangles, capturing a discrete analogue of curvature by detecting how gradients twist around vertices where multiple cells meet. In a concrete example of three cells meeting at a vertex in a 2D mesh, this term identifies and penalizes configurations where the gradients rotate sharply, preferring arrangements where the function varies coherently across the junction. As the dimension p increases, the regularization captures progressively more subtle patterns of variation, with each term $\lambda_{pk} \langle \kappa_p u, L_p^k \kappa_p u \rangle_p$ measuring inconsistencies in how the function behaves around $(p + 1)$ -way intersections of cells.

The parameters λ_{pk} provide fine-grained control over the regularization, allowing different weights for different dimensions p and different powers k of the Laplacian operator. The use of powers L_p^k enables control over higher-order smoothness within each dimension, analogous to penalizing higher derivatives in classical spline theory. This multi-scale framework naturally adapts to the geometric structure of the partition, applying appropriate smoothness constraints based on how cells meet and interact within the simplicial complex.

The minimizer of this functional satisfies the linear system:

$$\left(I + \sum_{p,k} \lambda_{pk} \kappa_p^* W_p L_p^{k-1} \kappa_p \right) u = y$$

This system, derived by setting the Fréchet derivative of \mathcal{E} to zero, has an intuitive structure despite its complex appearance. The operator on the left decomposes as:

$$\underbrace{I}_{\text{identity}} + \underbrace{\sum_{p,k} \lambda_{pk} \kappa_p^* W_p L_p^{k-1} \kappa_p}_{\text{weighted smoothing operators}}$$

Each term in the sum implements a specific type of smoothing: the operator κ_p lifts the vertex function to p -dimensional structures, L_p^{k-1} applies $(k - 1)$ -fold smoothing at that dimension, W_p incorporates the Riemannian metric weights, and κ_p^* projects the smoothed result back to vertices. The matrix W_p encodes the full geometric structure of the complex. For $p = 1$, this includes not just edge lengths but also the inner products between edges meeting at vertices, which involve both boundary areas and dihedral angles. For $p = 2$ and higher, W_p similarly captures volumes and relative orientations of higher-dimensional simplices. This rich geometric encoding ensures that the smoothing respects not just the sizes of cells but also their angular relationships in space.

To understand this concretely, consider the simplest case with only first-order edge smoothing ($p = 1, k = 1$):

$$(I + \lambda_{10} \kappa_1^* W_1 \kappa_1) u = y$$

Here, $\kappa_1 u$ computes discrete gradients on edges. The matrix W_1 incorporates the full Riemannian structure: diagonal entries contain edge weights (derived from boundary areas), while off-diagonal entries encode angular relationships through terms like

$$\sqrt{\text{vol}_{n-1}(F_{ij}) \cdot \text{vol}_{n-1}(F_{ik})} \cos \theta_{jk}.$$

The operator κ_1^* then aggregates these geometrically-weighted gradients back to vertices.

The higher-order terms (L_p^{k-1} with $k > 1$) enable control over smoothness derivatives. Just as classical splines can penalize not just function values but also derivatives and higher-order variations, these terms penalize higher-order roughness at each dimensional scale. The key advantage of this formulation is that despite the sophisticated multi-scale smoothing it encodes, the final system remains linear in the vertex values u , enabling efficient solution using standard sparse linear solvers. The complexity in the formula directly addresses our motivating challenge: incorporating geometric information beyond simple adjacency to achieve smoothing that respects how cells meet in space.

Returning to our example of three cells meeting at a vertex, the extended Laplacian and simplicial splines now provide geometrically-aware smoothing. If the cells meet symmetrically, the smoothing preserves this symmetry. If two cells form a narrow wedge against a third, the smoothing respects this anisotropy. The higher-dimensional terms automatically adapt to the local geometry, providing smoothing that graph-based methods cannot achieve.

These constructions demonstrate that smoothing operators can be systematically extended to incorporate higher-order geometric relationships. The lifting procedure provides a concrete mechanism for moving from vertex functions to higher-dimensional structures where multi-way interactions become accessible to standard differential operators. While the mathematical framework requires careful development, the resulting operators admit efficient implementation through linear systems on vertex functions.

The extended Laplacian and simplicial spline frameworks developed here offer one approach to incorporating geometric information in the refinement of partition models. The empirical validation of these refinement techniques across diverse domains constitutes an important direction for future research. This geometric perspective provides an alternative view where generalization might be related to the geometric structures induced by partition models rather than solely to model complexity.

2.4 Toward Density-Weighted Geometry and Curvature Perspectives

Consider two decision trees trained on different datasets that happen to create geometrically identical partitions of the ambient feature space. Both achieve similar training accuracy,

both induce identical simplicial complexes, and both have identical Riemannian metrics encoding boundary areas and dihedral angles. Yet one generalizes well to test data while the other overfits significantly. What distinguishes them?

One possible explanation involves how the geometry aligns with the underlying data distribution. A partition cell containing thousands of training points carries different statistical weight than an equally-sized cell containing just a few points. A boundary cutting through a dense cluster of data points has different implications than one passing through empty space. The Riemannian structure we have developed, while capturing rich geometric information, does not explicitly account for this statistical structure.

This limitation becomes evident when analyzing failure modes of machine learning models. Adversarial examples may exploit regions of low data density where models must extrapolate. Overfitting can manifest as excessive geometric complexity in sparsely populated regions. Transfer learning performance may depend on whether source and target domains share similar density patterns along with geometric features. These observations suggest that understanding machine learning models may benefit from integrating geometric and statistical perspectives.

How might we enrich our geometric framework to incorporate data density? One natural approach draws inspiration from physics, where density-weighted metrics appear in general relativity [68] and fluid dynamics [4]. In these contexts, the presence of matter or energy warps the underlying geometry, creating a unified geometric-physical structure. Similarly, we can modify our Riemannian metric on simplicial complexes to reflect data density, making paths through high-density regions effectively "shorter" than those through sparse regions.

This density weighting modifies the geometric analysis. Shortest paths now follow data concentrations rather than geometric geodesics. The notion of distance becomes statistical as well as geometric, opening the possibility of defining curvature-like measures that capture how models adapt to sparse, structured data.

This section develops these ideas systematically. We begin by incorporating statistical structure through density-weighted metrics (Section 2.4.1). We then develop discrete curvature measures that quantify how cell arrangements create effective curvature (Section 2.4.2). Building on these foundations, we introduce statistical Ricci curvature for edges of the simplicial complex, enabling a Taylor-like regularization framework that penalizes both local vertex irregularities and relational edge irregularities (Section 2.4.3). Finally, we examine how these geometric structures evolve during training, providing diagnostic tools for learning algorithms (Section 2.4.4).

The framework presented here is exploratory, offering new perspectives on familiar phenomena. By revealing the geometry that emerges from the interaction between sparse data and model partitions, we aim to contribute to the understanding of generalization, robustness, and learning dynamics in machine learning models. The geometric tools we develop raise intriguing questions: Might different architectures induce characteristic curvature patterns that explain their inductive biases and failure modes? How do geometric structures evolve during training, and can this evolution predict generalization performance? While these questions remain open, they suggest potentially fruitful connections between discrete geometry and machine learning.

2.4.1 Incorporating Statistical Structure

To incorporate data density into our geometric framework, we must first estimate how data distributes across the simplicial complex. Each cell C_i contains some number of training points $n_i = |\{x_j : x_j \in C_i\}|$. These raw counts provide a discrete, piecewise constant density estimate: $\tilde{\rho}_i = n_i/\text{vol}(C_i)$. However, such estimates are unstable in small cells and undefined in cells containing no data. We need a principled approach to smooth these estimates while respecting the geometric structure. We first show how to estimate density at vertices through a regularized optimization that balances data fidelity with smoothness constraints. With vertex densities established, we then face the challenge of extending these values to edges and higher-dimensional simplices. Simply averaging vertex densities ignores the rich geometric information encoded in our Riemannian structure. We explore several principled alternatives that incorporate geometric correction factors, each with different properties suited to particular applications.

The simplicial spline framework from Section 2.3 offers one possible approach. We seek a density function $\rho : V \rightarrow \mathbb{R}_+$ that minimizes:

$$\mathcal{E}[\rho] = \sum_{i \in V} \frac{(n_i - \text{vol}(C_i) \cdot \rho(v_i))^2}{\text{vol}(C_i)} + \lambda \sum_{p=0}^d \sum_{k=1}^{K_p} \langle \kappa_p \rho, L_p^k \kappa_p \rho \rangle_p$$

The first term ensures that density times volume approximates the observed counts, while the regularization term promotes smoothness across the simplicial complex. The weighting by $1/\text{vol}(C_i)$ gives equal importance to cells of different sizes, preventing large cells from dominating the optimization. This formulation naturally handles the common situation where some cells contain no training points, interpolating density from neighboring cells through the geometric structure.

The solution to this variational problem satisfies a linear system analogous to that for simplicial splines:

$$\left(D + \lambda \sum_{p,k} \kappa_p^* W_p L_p^{k-1} \kappa_p \right) \rho = Dn$$

where D is diagonal with $D_{ii} = 1/\text{vol}(C_i)$ and n is the vector of point counts. The multi-scale regularization through powers of the Hodge Laplacian ensures that density estimates vary smoothly while respecting the simplicial structure.

With vertex densities estimated, we must extend these values to edges and higher-dimensional simplices. The simplest approach would average vertex densities:

$$\rho(e) = \frac{\rho(v_i) + \rho(v_j)}{2}$$

for an edge $e = v_i \wedge v_j$. However, this ignores the geometric information encoded in our Riemannian structure. We propose incorporating a geometric correction factor:

$$\rho(e) = \frac{\rho(v_i) + \rho(v_j)}{2} \cdot \omega(e)$$

where

$$\omega(e) = \frac{\langle e, e \rangle^{1/2}}{\text{vol}_{n-1}(F_{ij})^{1/(n-1)}}$$

This correction factor is motivated by considering how edge lengths relate to boundary geometry. The numerator $\langle e, e \rangle^{1/2}$ is the edge length in our Riemannian structure, which by the compatibility conditions is the same whether computed at vertex v_i or v_j . The denominator $\text{vol}_{n-1}(F_{ij})^{1/(n-1)}$ represents an "expected" length based on the boundary area between cells. In regular geometries, when a polytope is scaled by factor λ , edge lengths scale by λ while $(n-1)$ -dimensional boundaries scale by λ^{n-1} , so edge length scales as the $(n-1)$ -th root of boundary volume. The ratio $\omega(e)$ thus compares the actual edge length to this expected scale.

When $\omega(e) > 1$, the edge is effectively "stretched" in the Riemannian metric relative to its boundary size, suggesting this connection carries more geometric significance. We accordingly increase the density estimate along this edge. Conversely, when $\omega(e) < 1$, the edge is "compressed," indicating less geometric importance, and we decrease the density estimate. This approach aims to incorporate both statistical and geometric structure in the density interpolation.

The choice of this particular extension deserves scrutiny, as several mathematically principled alternatives exist. The formula above uses arithmetic averaging with a geometric correction factor, but other approaches may prove more suitable depending on the application: The harmonic interpolation approach would define edge density using the harmonic mean:

$$\rho_{\text{harm}}(e) = \frac{2\rho(v_i)\rho(v_j)}{\rho(v_i) + \rho(v_j)} \cdot \omega(e)$$

The harmonic mean naturally appears when considering conductances in parallel. Recall that when two resistors with resistances R_1 and R_2 are connected in parallel, the combined resistance R is:

$$\frac{1}{R} = \frac{1}{R_1} + \frac{1}{R_2}.$$

Converting to conductances $G = 1/R$, this becomes simply:

$$G = G_1 + G_2$$

So conductances add in parallel. The combined resistance is:

$$R = \frac{R_1 R_2}{R_1 + R_2} = \frac{1}{\frac{1}{R_1} + \frac{1}{R_2}}.$$

This is half the harmonic mean of R_1 and R_2 . This connection makes the harmonic mean natural for resistor network analogies [62]. This choice tends to be more sensitive to low-density regions, making paths avoid sparse areas more strongly.

Alternatively, we could use the lifting operator framework more directly. Since $\kappa_1(\rho)$ lifts the density function to edges, we might define:

$$\rho_{\text{lift}}(e) = \kappa_1(\rho)(e) = \frac{\text{vol}_{n-1}(F_{ij})}{\text{vol}(C_i) + \text{vol}(C_j)} \cdot (\rho(v_i) + \rho(v_j))$$

This approach weights the contribution of each vertex by its cell’s relative size, naturally handling cases where adjacent cells have very different volumes.

A geometric mean approach suggests:

$$\rho_{\text{geom}}(e) = \sqrt{\rho(v_i) \cdot \rho(v_j) \cdot \omega(e)}$$

This formulation has the advantage of being scale-invariant under simultaneous scaling of densities, properties that may be desirable in certain contexts.

Each approach has different mathematical properties that may be relevant for the resulting density-weighted metric. The arithmetic mean treats densities linearly, the harmonic mean gives more weight to smaller values (as seen in the resistor network analogy), the lifting-based approach explicitly incorporates cell volumes into the weighting, and the geometric mean preserves multiplicative relationships between densities. The appropriate choice likely depends on the specific machine learning context and the phenomena being studied. This multiplicity of mathematically principled definitions underscores the exploratory nature of this framework and invites empirical investigation to determine which formulation best captures the relationship between data density and model behavior.

The incorporation of density fundamentally alters our notion of distance on the simplicial complex. Drawing inspiration from optimal transport theory [66, 54] and information geometry [3], we define a density-weighted metric:

$$d_\rho(e) = \frac{\ell(e)}{\rho(e)^\alpha}$$

where $\ell(e)$ is the original Riemannian length of edge e and $\alpha \in (0, 1]$ controls the strength of density weighting. This modification makes paths through high-density regions effectively shorter than those through sparse regions.

This modification of the metric has significant geometric consequences. Shortest paths no longer follow geometric geodesics but instead curve toward data concentrations. The distance between two vertices now depends not just on their geometric separation but on the density of data along connecting paths. This aligns with the intuition that model behavior in dense regions is more reliable and should influence distant predictions more strongly than sparse regions.

Consider how this density weighting affects the analysis of our earlier example. The boundary between cells C_1 (with 1,000 points) and C_2 (with 10 points) now carries different weight than a boundary between two dense cells. Paths that venture into the sparse cell C_2 become longer under the density-weighted metric, reflecting the increased uncertainty in that region. The simplicial complex retains its combinatorial structure, but the effective geometry warps to reflect statistical confidence.

This density-weighted geometric framework provides the foundation for studying how machine learning models adapt to data distributions. By enriching the Riemannian structure with statistical information, we create a unified geometric-statistical object that captures both the partition structure and its relationship to data. The stage is now set for exploring how this enriched geometry might exhibit forms of curvature that explain model behavior, a possibility we explore in the following sections.

2.4.2 Vertex-based Curvatures for ML Models

The density-weighted metric introduced in Section 2.4.1 opens the possibility of defining curvature-like measures for machine learning models. Yet this possibility immediately confronts us with a paradox: the partitions created by these models divide Euclidean space into convex polytopes, each inheriting the flat geometry of the ambient space. There is no intrinsic curvature in the classical sense. Paths within cells follow straight lines, and parallel transport around any loop returns vectors unchanged. How then can we speak meaningfully of curvature?

The resolution lies in recognizing that real-world data, despite living in high-dimensional Euclidean space, is typically sparse and highly structured. This sparsity and non-uniform distribution effectively creates geometric curvature through the arrangement of partition cells. When data concentrates in specific regions or along lower-dimensional structures while leaving vast regions empty, machine learning models must adapt their partitions to this inhomogeneous structure. The resulting configuration of cells exhibits curvature-like properties that emerge not from the geometry within cells, but from how the cells are arranged and connected, much like how a geodesic dome exhibits global curvature despite being built from flat triangular panels. We seek to explore whether these curvature-like properties relate to model behavior, generalization, and robustness through the curvature measures developed below.

Data Geometry Based Vertex Curvatures We begin by developing curvature measures that capture how the arrangement of cells responds to data density. These measures exploit the density-weighted metric introduced in Section 2.4.1 to quantify various geometric phenomena at vertices: how quickly neighborhoods grow, how geodesics spread, and how paths navigate through the cell structure. Each measure captures a different aspect of the effective geometry created by sparse data.

The most direct approach examines the growth rate of density-weighted balls. Under the density-weighted metric, the distance between points depends on data density along connecting paths. For a vertex v in our simplicial complex, define the density-weighted ball of radius r :

$$\mathcal{B}_r^\rho(v) = \{w \in V : d_\rho^{\text{geodesic}}(v, w) \leq r\}$$

where d_ρ^{geodesic} is the shortest path distance using the density-weighted metric.

In flat space with uniform density, we expect $|\mathcal{B}_r^\rho(v)|$ to grow as r^n . Deviations from this growth rate indicate curvature. Define the discrete ball-growth curvature at scale r as:

$$\kappa_r^{\text{ball}}(v) = \frac{N_r(v) - N_r^{\text{flat}}(v)}{N_r^{\text{flat}}(v)}$$

where $N_r(v) = |\mathcal{B}_r^\rho(v)|$ is the actual number of vertices in the ball and $N_r^{\text{flat}}(v) = \rho(v) \cdot V_n \cdot r^n$ is the expected number in flat space with uniform density $\rho(v)$, where V_n is the volume of the unit ball in \mathbb{R}^n .

This definition exhibits clear geometric meaning. When $\kappa_r^{\text{ball}}(v) > 0$, the ball contains more vertices than expected, suggesting positive curvature where geodesics emanating from v

converge back together. When $\kappa_r^{\text{ball}}(v) < 0$, geodesics diverge more rapidly than in flat space, indicating negative curvature. The scale parameter r allows us to probe curvature at different resolutions, from local perturbations to global structure.

A different approach to local curvature examines distance deviations in the immediate neighborhood. Define the distance-deviation curvature as:

$$\kappa^{\text{dist}}(v) = 1 - \frac{\sum_{w \in \partial \overline{\text{Star}}(v)} d_\rho(v, w)}{|\partial \overline{\text{Star}}(v)| \cdot \bar{d}_\rho}$$

where $\partial \overline{\text{Star}}(v)$ denotes the set of vertices adjacent to v and $|\partial \overline{\text{Star}}(v)|$ is the number of such vertices (the degree of v) and \bar{d}_ρ is a characteristic distance scale in the complex. This measures whether neighbors are systematically closer (positive curvature) or farther (negative curvature) than typical.

Another geometric approach examines how geodesics spread as they emanate from a vertex, adapting the notion of Jacobi fields to the discrete setting. In smooth Riemannian geometry, the spreading of geodesics is governed by the Jacobi equation, with positive curvature causing convergence and negative curvature causing divergence [26, 41].

For our discrete setting, we introduce geodesic spray analysis to measure this spreading. Consider all vertices at density-weighted distance r from vertex v , forming the discrete sphere:

$$\mathcal{S}_r^\rho(v) = \{w : d_\rho^{\text{geodesic}}(v, w) = r\}$$

For each $w \in \mathcal{S}_r^\rho(v)$, let γ_{vw} be a shortest path from v to w . We measure geodesic spreading through two complementary approaches.

The first measures angular spread at the source by examining initial directions:

$$\Theta_r^{\text{angle}}(v) = \frac{1}{|\mathcal{S}_r^\rho(v)|^2} \sum_{w, w' \in \mathcal{S}_r^\rho(v)} \angle_v(w, w')$$

where $\angle_v(w, w')$ is the angle between the first edges of paths γ_{vw} and $\gamma_{vw'}$, computed using the Riemannian inner product:

$$\cos(\angle_v(w, w')) = \frac{\langle e_w, e_{w'} \rangle_v}{\|e_w\|_v \|e_{w'}\|_v}$$

The second, more global measure examines how far apart geodesics end up after traveling distance r :

$$\Theta_r^{\text{spread}}(v) = \frac{\sum_{w, w' \in \mathcal{S}_r^\rho(v)} d_\rho^{\text{geodesic}}(w, w')}{|\mathcal{S}_r^\rho(v)|^2 \cdot 2r}$$

To convert these spreading measures to curvatures, we compare to expected values in flat space. Define the geodesic spreading curvature as:

$$\kappa_r^{\text{spray}}(v) = 1 - \Theta_r^{\text{spread}}(v)$$

When $\kappa_r^{\text{spray}}(v) > 0$, geodesics converge (positive curvature). When $\kappa_r^{\text{spray}}(v) < 0$, geodesics diverge more than expected (negative curvature).

A different local curvature measure examines triangular relationships in the immediate neighborhood. Define the triangle-based curvature as:

$$\kappa^{\text{tri}}(v) = \frac{1}{|\partial\overline{\text{Star}}(v)|^2} \sum_{w,w' \in \partial\overline{\text{Star}}(v)} \left(1 - \frac{d_\rho(w, w')}{d_\rho(v, w) + d_\rho(v, w')} \right)$$

This measures whether the triangle inequality is tight (zero curvature) or loose (positive curvature indicates neighbors are closer than the sum of distances through v).

While these spreading measures capture how geodesics diverge or converge, they do not reveal the complexity of the paths themselves. A third approach examines how geodesics navigate through the partition structure.

For vertices at distance r from v , define the path complexity measure:

$$J_r(v) = \frac{1}{|\mathcal{S}_r^\rho(v)|} \sum_{w \in \mathcal{S}_r^\rho(v)} \frac{|\gamma_{vw}|_{\text{cells}}}{r}$$

where $|\gamma_{vw}|_{\text{cells}}$ counts the number of distinct cells the path traverses. In flat space with uniform density, we expect paths to traverse a number of cells proportional to their length, giving $J_r(v) \approx 1/\bar{\ell}$ where $\bar{\ell}$ is the average cell diameter.

Define the path complexity curvature as:

$$\kappa_r^{\text{path}}(v) = J_r(v) \cdot \bar{\ell} - 1$$

When $\kappa_r^{\text{path}}(v) > 0$, geodesics wind through more cells than expected, indicating complex local structure or fragmented partitions. When $\kappa_r^{\text{path}}(v) < 0$, paths traverse fewer cells, suggesting larger, more regular cells in that region.

Functional Curvature at Vertices While the data based curvatures capture geometric structure of the underlying partitions, machine learning models are ultimately function approximators and understanding their behavior requires not just geometric but also functional analysis. How can we extend curvature concepts to the functions defined on our partition complexes?

Traditional regularization approaches penalize gradient magnitudes through L1 or L2 norms, but these measures are inherently positive and miss the fundamental signed nature of curvature. A function that oscillates wildly between convex and concave behavior differs qualitatively from one that maintains consistent convexity, yet gradient norms alone cannot distinguish these cases. This limitation motivates the development of functional curvature measures that capture both the magnitude and sign of local function behavior.

We propose several complementary approaches to functional curvature, each capturing different aspects of how functions behave on simplicial complexes. The most direct approach adapts the classical mean curvature through the graph Laplacian. For a function f defined on vertices, the discrete mean curvature at vertex v takes the form

$$\kappa_f^{\text{mean}}(v) = \frac{\Delta f(v)}{f(v) - \bar{f}_v}$$

where

$$\Delta f(v) = \sum_{w \sim v} w_{vw} (f(w) - f(v))$$

is the weighted graph Laplacian and

$$\bar{f}_v = \frac{\sum_{w \sim v} w_{vw} f(w)}{\sum_{w \sim v} w_{vw}}$$

represents the weighted average of f over neighbors. This ratio captures whether f is locally convex (positive curvature) or concave (negative curvature) relative to its neighborhood average.

A more geometric approach examines gradient variations around vertices through an angle-based measure. For a vertex v , we define:

$$\kappa_f^{\text{angle}}(v) = \frac{1}{|E_v|(|E_v| - 1)} \sum_{e_i, e_j \in E_v, i \neq j} \log \left(\frac{1 + \cos \angle(\vec{\nabla} f|_{e_i}, \vec{\nabla} f|_{e_j})}{1 - \cos \angle(\vec{\nabla} f|_{e_i}, \vec{\nabla} f|_{e_j})} \right)$$

where E_v is the set of edges incident to v . For edge $e_i = v \wedge w_i$, we define the gradient vector of f along e_i as:

$$\vec{\nabla} f|_{e_i} = \frac{f(w_i) - f(v)}{\ell(e_i)^2} \cdot e_i$$

where we scale by $\ell(e_i)^2$ to account for the edge having length $\ell(e_i)$. The cosine of the angle between gradient vectors is:

$$\cos \angle(\vec{\nabla} f|_{e_i}, \vec{\nabla} f|_{e_j}) = \text{sign}((f(w_i) - f(v))(f(w_j) - f(v))) \cdot \frac{\langle e_i, e_j \rangle_v}{\ell(e_i) \cdot \ell(e_j)}$$

This measure ranges from $-\infty$ to $+\infty$, with values near zero indicating moderately varied gradient directions typical of regular points. Large positive values occur when gradients are strongly aligned, suggesting a local extremum where the function consistently increases or decreases in all directions. Large negative values indicate opposing gradients characteristic of saddle points, where the function increases in some directions while decreasing in others. The logarithmic formulation amplifies the distinction between aligned and opposing gradients, making it particularly sensitive to detecting extrema and saddle configurations.

For functions with sufficient regularity, we can examine the geometry of level sets through the discrete structure of the simplicial complex. The level set curvature at vertex v measures how the function deviates from linear behavior by examining the variance of directional derivatives:

$$\kappa_f^{\text{level}}(v) = \frac{1}{|\partial \text{Star}(v)|} \sum_{w \in \partial \text{Star}(v)} \left(\frac{f(w) - f(v)}{d(v, w)} - \langle \nabla f \rangle_v \right)^2$$

where $\partial \text{Star}(v)$ denotes the vertices in the star of v excluding v itself, $d(v, w)$ is the Riemannian distance between vertices, and

$$\langle \nabla f \rangle_v = \frac{1}{|\partial \text{Star}(v)|} \sum_{w \in \partial \text{Star}(v)} \frac{f(w) - f(v)}{d(v, w)}$$

is the average directional derivative. This measure captures how much the function’s rate of change varies in different directions emanating from v . When $\kappa_f^{\text{level}}(v) = 0$, the function behaves linearly in the star of v , while large values indicate that level sets bend significantly, suggesting local nonlinearity or saddle-like behavior in the function landscape.

Vertex Curvatures as Aggregations A crucial insight emerges when we examine how these vertex curvatures relate to edge-based information. The discrete mean curvature explicitly aggregates differences along edges through the Laplacian operator. The angle-based curvature aggregates angular information from pairs of edges. The level set curvature averages squared deviations of edge-based gradients.

This observation reveals that vertex curvatures, while providing valuable local diagnostics, inherently average away edge-specific information. A vertex might exhibit zero mean curvature because all neighboring values equal the average, or because positive and negative deviations cancel. The aggregation process loses information about which specific edges contribute to the curvature and how.

This limitation becomes particularly relevant when designing regularization strategies. Penalizing only vertex curvatures might miss pathological configurations where problems concentrate along specific edges or boundaries. Two models might have identical vertex curvature distributions while differing dramatically in their edge-level behavior.

Connecting to Model Phenomena These discrete curvature measures may connect to machine learning phenomena in several ways. We hypothesize that regions of positive geometric curvature, where density-weighted balls grow faster than expected, could correspond to stable predictions where the model’s behavior remains consistent across neighborhoods. Such regions might contain ample training data distributed uniformly, potentially allowing the model to learn robust patterns.

Similarly, negative geometric curvature regions, where geodesics diverge rapidly, might coincide with decision boundaries or areas of high model variance. The diverging geodesics could reflect how small perturbations lead to different predictions, which would be characteristic of regions where the model lacks confidence.

The functional curvatures suggest additional connections. High positive mean curvature might indicate local overfitting, where the model’s predictions form sharp peaks. Negative mean curvature could suggest underfitting, where the model fails to capture local patterns. Non-zero angle-based curvature might identify saddle points that could affect optimization or create vulnerabilities.

These potential connections between curvature measures and model behavior motivate further empirical investigation. The scale-dependence of these measures could prove particularly valuable for practical application. A vertex might exhibit positive curvature at small scales, suggesting local stability, while displaying negative curvature at larger scales, indicating its position within a complex global structure. This multi-scale analysis helps distinguish between local irregularities that might be smoothed and fundamental geometric features that should be preserved.

Computing these discrete curvature measures requires only local calculations on the simplicial complex, making them practical even for large models. The vertex-based nature allows parallel computation and efficient updates as the model evolves during training. These computational advantages, combined with their diagnostic value, make discrete curvatures valuable tools for understanding and improving machine learning models.

The framework developed in this section provides the foundation for more sophisticated geometric analysis. While vertex curvatures offer important local diagnostics, they aggregate edge-level information in ways that may obscure important relational structure. This observation motivates the development of edge-based curvature measures that can capture the fine-grained geometric relationships between model regions, a topic we explore in the following section.

2.4.3 Statistical Ricci Curvature and Geometric Regularization

The vertex-based curvatures developed in Section 2.4.2 provide valuable local diagnostics but inherently aggregate information from incident edges. This aggregation, while useful for understanding local behavior, obscures the fine-grained relational structure between cells that often determines model performance. Just as Taylor series expansions capture function behavior through derivatives of increasing order, we can construct regularization frameworks that incorporate geometric information at multiple scales of the simplicial complex.

Consider a general geometric regularization functional that expands over the dimensions of our simplicial complex:

$$R(f) = \sum_{p=0}^{\dim K} \lambda_p \sum_{\sigma \in K_p} \psi_p(\kappa_f^{\text{stat},p}(\sigma)),$$

where $\kappa_f^{\text{stat},p}(\sigma)$ represents a statistical curvature measure for a p -simplex σ , and ψ_p are penalty functions chosen based on the desired properties at each dimension. The $p = 0$ term captures vertex-based curvatures as developed in Section 2.4.2. Higher-order terms incorporate increasingly sophisticated relational information: edges ($p = 1$) capture pairwise relationships between cells, triangles ($p = 2$) encode three-way interactions, and so forth.

This Taylor-like expansion reveals a fundamental principle for geometric regularization. Just as truncating a Taylor series at first order often provides adequate approximation for smooth functions, considering only vertices and edges may suffice for many machine learning applications. The vertex term ensures local regularity, while the edge term captures the most important relational structure. Higher-order terms become relevant when complex multi-way interactions significantly impact model behavior.

For practical implementation, we focus on developing the $p = 1$ (edge) term, which provides the most important extension beyond vertex-based measures. This leads to the regularization framework:

$$R(f) = \sum_{v \in V} \phi(|\kappa_f^{\text{stat}}(v)|) + \lambda \sum_{(v,w) \in E} \psi((\kappa_f^{\text{stat}}(v,w))^2)$$

The remainder of this section develops the edge-based statistical curvature $\kappa_f^{\text{stat}}(v, w)$, showing how it captures relational properties that vertex measures miss.

Edge-Based Statistical Curvature Following the decomposition principle established for vertex curvatures, we define statistical Ricci curvature for an edge $e = v \wedge w$ as:

$$\text{Ric}_{\text{stat}}(v, w) = \text{Ric}_{\text{geom}}(v, w) + \text{Ric}_{\text{dens}}(v, w) + \text{Ric}_{\text{func}}(v, w)$$

This decomposition maintains the philosophy that statistical structure emerges from the interplay of geometric configuration, data distribution, and functional behavior, now applied to measuring relationships between cells rather than local properties.

Geometric Ricci Curvature The geometric component adapts Ollivier’s coarse Ricci curvature to our discrete setting. This elegant construction measures how neighborhoods of adjacent vertices relate to each other through optimal transport. For vertices v and w , we construct probability measures μ_v and μ_w supported on their respective neighbors, with weights proportional to edge lengths in the Riemannian metric:

$$\mu_v(u) = \frac{\langle v \wedge u, v \wedge u \rangle_v^{1/2}}{\sum_{u' \sim v} \langle v \wedge u', v \wedge u' \rangle_v^{1/2}}$$

The geometric Ricci curvature then measures how these probability distributions relate under optimal transport:

$$\text{Ric}_{\text{geom}}(v, w) = 1 - \frac{W_1(\mu_v, \mu_w)}{d_\rho(v, w)},$$

where W_1 denotes the Wasserstein-1 distance computed using our density-weighted metric. The interpretation follows classical intuition: positive values indicate that neighborhoods of v and w are more similar than their distance would suggest, implying local geometric regularity. The mass from μ_v can be transported to μ_w through paths shorter than expected, suggesting convergence of geodesics. Negative values indicate geometric divergence, where transporting mass requires longer paths than the direct distance would suggest.

This construction naturally incorporates the full Riemannian structure of our simplicial complex. The edge weights in the probability measures reflect boundary areas and dihedral angles, while the density-weighted metric in the Wasserstein distance accounts for data distribution. The result is a geometrically and statistically aware measure of local curvature that respects the rich structure of our partition complex.

Density Ricci Curvature The density component captures how data concentration varies along edges. In smooth Riemannian geometry, Ricci curvature relates to the second derivative of volume growth. Adapting this principle to our discrete setting, we measure the convexity of density along an edge:

$$\text{Ric}_{\text{dens}}(v, w) = \frac{2}{\rho(e)} \left(\frac{\rho(v) + \rho(w)}{2} - \rho(e) \right)$$

The edge density $\rho(e)$ comes from our interpolation scheme developed in Section 2.4.1, which incorporates geometric correction factors to respect the Riemannian structure. When density is convex along the edge (the midpoint density exceeds the average of endpoint densities), we obtain positive curvature, suggesting smooth data distribution. Negative values indicate concave density, potentially signaling a boundary cutting through a data cluster.

This measure could prove valuable for detecting problematic partition boundaries. A decision boundary that slices through a dense cluster of similar points will exhibit strongly negative density curvature, while boundaries that respect natural data groupings show near-zero or positive values. This diagnostic capability makes density curvature a powerful tool for understanding model behavior.

Functional Ricci Curvature The functional component quantifies how model predictions transition between cells. For the general case where models may have different functional forms in adjacent cells, we need to measure the consistency of model behavior across boundaries. We define different functional curvature measures to capture different aspects of functional behavior across adjacent cells.

The mean curvature component measures consistency of local convexity:

$$\text{Ric}_{\text{func}}^{\text{mean}}(v, w) = 1 - \frac{|\kappa_f(v) - \kappa_f(w)|}{|\kappa_f(v)| + |\kappa_f(w)| + \epsilon}$$

where κ_f is the discrete mean curvature from Section 2.4.2 and $\epsilon > 0$ is a small regularization parameter that prevents division by zero when both vertices have near-zero curvature. This captures whether the function maintains consistent local behavior along the edge, with values close to 1 indicating smooth transitions between regions of similar curvature and negative values suggesting abrupt changes from convex to concave behavior.

The level set component examines how directional derivative variance changes:

$$\text{Ric}_{\text{func}}^{\text{level}}(v, w) = 1 - \frac{\sqrt{\kappa_f^{\text{level}}(v)} + \sqrt{\kappa_f^{\text{level}}(w)}}{2} \cdot \frac{|f(v) - f(w)|}{d_\rho(v, w) \cdot \|\nabla f\|_{\text{avg}}}$$

where $\|\nabla f\|_{\text{avg}} = \frac{1}{|E|} \sum_{(u, u') \in E} \frac{|f(u) - f(u')|}{d_\rho(u, u')}$ represents the average gradient magnitude across all edges in the simplicial complex. This normalization factor ensures the measure is scale-invariant and combines local nonlinearity (through the level set curvatures) with the rate of change along the edge relative to the global gradient behavior.

For models with continuous predictions across cells, we also include a direct measure of gradient discontinuity:

$$\text{Ric}_{\text{func}}^{\text{direct}}(v, w) = 1 - \beta \frac{\int_{C_v \cap C_w} \|\nabla f_v - \nabla f_w\|^2 d\sigma}{\text{vol}_{n-1}(C_v \cap C_w) \cdot \|\nabla f\|_{\text{avg}}^2}$$

where $\beta > 0$ is a scaling parameter. Since the fraction measures the squared gradient jump relative to the average squared gradient, it can range from 0 (perfect continuity) to values exceeding 1 (opposing gradients). A natural choice would be $\beta \in [0.25, 1]$ to ensure the

functional Ricci curvature remains appropriately bounded and comparable to the other components. For piecewise constant models, this reduces to:

$$\text{Ric}_{\text{func}}^{\text{direct}}(v, w) = 1 - \gamma \frac{\|c_v - c_w\|^2}{\|c_v\|^2 + \|c_w\|^2}$$

where $\gamma > 0$ similarly provides scaling, with the choice of γ depending on the desired sensitivity to prediction discontinuities across cell boundaries.

The components above measure intrinsic properties of the function f . We can also directly measure how well the model predictions align with the training responses across the edge:

$$\text{Ric}_{\text{func}}^{\text{response}}(v, w) = 1 - \frac{\sum_{x_k \in C_v \cup C_w} |f(x_k) - y_k|^2}{\sum_{x_k \in C_v \cup C_w} |y_k - \bar{y}|^2}$$

where $\bar{y} = \frac{1}{|C_v \cup C_w|} \sum_{x_k \in C_v \cup C_w} y_k$ is the mean response over the data points in the two cells. This measures prediction accuracy relative to the variance in the data, with values near 1 indicating good local fit.

The functional Ricci curvature can be defined as a weighted combination:

$$\text{Ric}_{\text{func}}(v, w) = \alpha_1 \text{Ric}_{\text{func}}^{\text{mean}}(v, w) + \alpha_2 \text{Ric}_{\text{func}}^{\text{level}}(v, w) + \alpha_3 \text{Ric}_{\text{func}}^{\text{direct}}(v, w) + \alpha_4 \text{Ric}_{\text{func}}^{\text{response}}(v, w)$$

where the weights α_i represent a design choice in the regularization framework. Different weight configurations emphasize different aspects: setting only $\alpha_4 = 1$ focuses on prediction accuracy, while including other components incorporates smoothness and consistency properties.

Regularization Through Geometric Penalties With the statistical Ricci curvature fully developed, we can now complete the regularization framework:

$$R(f) = \sum_{v \in V} \phi(\kappa_f^{\text{stat}}(v)) + \lambda \sum_{(v,w) \in E} \psi(\text{Ric}_{\text{stat}}(v, w))$$

The vertex term penalizes extreme local curvatures while allowing moderate values that may represent legitimate data structure. The edge term penalizes poor transitions between cells, encouraging models that respect both geometric and statistical structure. The balance parameter λ controls the relative importance of local versus relational regularity.

The choice of penalty functions ϕ and ψ depends on the specific application and desired properties. For robust regularization that allows some geometric variation while preventing extremes, one might choose:

$$\phi(x) = \begin{cases} x^2 & \text{if } |x| \leq \tau \\ 2\tau|x| - \tau^2 & \text{if } |x| > \tau \end{cases}$$

This Huber-like penalty transitions from quadratic to linear, preventing single high-curvature vertices from dominating the regularization. For edges, a simpler quadratic penalty $\psi(x) = x^2$ may suffice, though the relative stability and informativeness of edge curvatures requires empirical validation.

Computational Considerations Computing statistical Ricci curvature requires several geometric quantities that can be efficiently maintained during model training. The Wasserstein-1 distance for geometric curvature can be computed using linear programming for small vertex degrees or approximated using entropic regularization for larger problems. The density interpolation requires solving the linear system from Section 2.4.1 once per training epoch or when the partition structure changes significantly.

For neural networks, the partition structure changes discretely when activation patterns shift. Rather than recomputing all curvatures from scratch, we can maintain incremental updates for affected edges. When a hyperplane shifts slightly without changing the combinatorial structure, curvatures can be updated through sensitivity analysis. This incremental approach makes geometric regularization practical even for large models.

Higher-Order Terms The Taylor-like expansion in principle accommodates higher-order simplices beyond edges. For triangles ($p = 2$) and higher-dimensional simplices, one could define analogous curvature measures that capture multi-way interactions among cells. The diagnostic value and practical benefit of these higher-order terms for machine learning applications remains an open question. We conjecture that for many applications, the combination of vertex and edge terms may be sufficient to capture the essential geometric structure.

Geometric Monitoring During Training The statistical curvature framework enables practical tools for monitoring and improving model training. As parameters evolve during optimization, they induce changes in the partition structure and corresponding geometric quantities:

$$\theta(t) \xrightarrow{\text{determines}} \mathcal{P}(t) \xrightarrow{\text{induces}} K(t) \xrightarrow{\text{equipped with}} (\langle \cdot, \cdot \rangle(t), \rho(t), \{f_\alpha(t)\})$$

By tracking these geometric measures, we may gain insights complementary to traditional loss-based monitoring.

A comprehensive geometric diagnostic tracks the distribution of curvatures across the model:

$$\mathcal{C}(t) = \{\kappa_f^{\text{stat}}(v, t) : v \in V(t)\} \cup \{\text{Ric}_{\text{stat}}(v, w, t) : (v, w) \in E(t)\}$$

We hypothesize that early in training, highly variable curvatures with many extreme values would be observed. As training progresses, the distribution might stabilize if the model is learning appropriate geometric structure. A sudden increase in negative curvatures could potentially provide an early warning signal of overfitting.

The geometric energy provides a scalar summary of overall geometric irregularity:

$$E(t) = \sum_{v \in V(t)} (\kappa_f^{\text{stat}}(v, t))^2 \cdot \text{vol}_n(C_v) + \lambda \sum_{(v, w) \in E(t)} (\text{Ric}_{\text{stat}}(v, w, t))^2 \cdot \text{vol}_{n-1}(F_{vw})$$

Monitoring this energy might reveal phases of learning: rapid decrease during initial structure discovery, stabilization during fitting, and potential increase if overfitting begins. Beyond passive monitoring, these geometric insights could actively guide optimization.

For adaptive optimization, we propose adjusting learning rates based on how strongly each parameter affects the geometric structure. If changing parameter θ_i causes large changes in curvature values throughout the model, this parameter might benefit from a smaller learning rate to avoid destabilizing the geometry. Specifically, we could set:

$$\eta_i(t) = \eta_{\text{base}} \cdot g \left(\sum_{v \in V} \left| \frac{\partial \kappa_f^{\text{stat}}(v, t)}{\partial \theta_i} \right| + \sum_{(v, w) \in E} \left| \frac{\partial \text{Ric}_{\text{stat}}(v, w, t)}{\partial \theta_i} \right| \right)$$

where the sum measures the total sensitivity of all curvatures to parameter θ_i . The function g is decreasing (for example, $g(x) = 1/(1+x)$), so parameters with high geometric sensitivity get smaller learning rates. This could help prevent training instabilities caused by rapid geometric changes.

For ensemble methods like gradient boosting, the geometric perspective could reveal how models sequentially refine partitions. Each new weak learner modifies the combined partition, with co-occurrence frequencies evolving as:

$$K^{(m+1)}(C_i, C_j) = \frac{m \cdot K^{(m)}(C_i, C_j) + \mathbf{1}[\text{adjacent in tree } m + 1]}{m + 1}$$

Monitoring whether these frequencies converge (potentially indicating geometric consensus) or diverge (possibly suggesting inconsistent structures) might provide insight into ensemble behavior beyond prediction accuracy.

These geometric monitoring tools could complement traditional metrics, potentially revealing when models transition from learning robust patterns to memorizing noise, even before validation performance degrades.

2.4.4 Open Questions and Future Directions

While the geometric monitoring tools developed above offer immediate practical applications, they also point toward deeper questions about the nature of learning in machine learning models.

The relationship between geometry and learning extends beyond monitoring to fundamental questions about architecture and regularization. Different architectures create distinct initial geometric structures that constrain how partitions can evolve during training. Understanding these constraints might inform architecture design, considering not only expressiveness but also geometric properties that affect learning dynamics.

Existing regularization techniques like dropout, weight decay, and batch normalization demonstrably improve generalization, but their geometric effects remain unclear. These methods might implicitly modify the evolution of partition geometry to avoid problematic configurations. Alternatively, one could consider regularization that explicitly targets geometric pathologies identified through curvature analysis.

The relationship between statistical Ricci curvature and generalization bounds presents another open question. Classical learning theory relies on complexity measures such as

VC dimension [65, 64] and Rademacher complexity [6, 48]. Models with bounded statistical Ricci curvature throughout training might achieve different generalization properties, offering an alternative perspective to classical measures.

These questions invite investigation from both theoretical and empirical perspectives. Validating geometric insights requires careful experimentation across diverse architectures and tasks. The connections between discrete geometry and machine learning suggested here remain largely conjectural, awaiting systematic exploration.

3. The Geometry of Feed-forward Networks

In the previous section, we saw how partition models naturally induce Riemannian simplicial complexes. Given data points $x_1, x_2, \dots, x_N \in \mathbb{R}^n$ and responses $y_1, y_2, \dots, y_N \in \mathbb{R}$, the geometry of the partition \mathcal{P} of a partition model is encapsulated by a nerve simplicial complex $K(\mathcal{P})$ equipped with a Riemannian structure $\langle \cdot, \cdot \rangle_{\mathcal{P}}$. Can neural networks be understood through this same geometric lens?

Feed-forward networks represent the simplest architecture in deep learning. While their expressive power has been well-studied [55, 10], in this section we show that they also give rise to rich geometric structures of functionally enriched Riemannian simplicial complexes: geometric objects that encode both the combinatorial structure of the network’s partitions and the affine transformations it applies within each region. Moreover, while tree-based models create a single partition, neural networks generate a sequence of increasingly refined partitions through their layers.

Consider the fundamental challenge: a neural network transforms data through multiple layers, each creating its own geometric structure. How do these structures relate to each other, and can we track geometric information as it flows through the network? To answer this question, we begin with the simplest building block—individual neurons—and progressively build our understanding of how layers compose these geometric structures.

A single perceptron provides our starting point. Given a bounded domain $\mathcal{D} \subset \mathbb{R}^n$, a perceptron is a mapping

$$\rho : \mathcal{D} \rightarrow \mathbb{R}$$

defined by

$$\rho(\mathbf{x}) = \sigma(\mathbf{w}^T \mathbf{x} + b),$$

where $\mathbf{w} \in \mathbb{R}^n$ is the weight vector, $b \in \mathbb{R}$ is the bias, and σ is an activation function. The hyperplane $H = \{\mathbf{x} : \mathbf{w}^T \mathbf{x} + b = 0\}$ divides \mathbb{R}^n into two half-spaces:

$$H^+ = \{\mathbf{x} : \mathbf{w}^T \mathbf{x} + b > 0\},$$

and

$$H^- = \{\mathbf{x} : \mathbf{w}^T \mathbf{x} + b \leq 0\}.$$

This division induces a partition $\mathcal{P} = \{C_1, C_2\}$ of our domain, where $C_1 = H^+ \cap \mathcal{D}$ and $C_2 = H^- \cap \mathcal{D}$, and the set of local prediction functions

$$\mathcal{F} = \{f_1 = \rho|_{C_1} : C_1 \rightarrow \mathbb{R}, f_2 = \rho|_{C_2} : C_2 \rightarrow \mathbb{R}\}$$

For the ReLU activation function, the neuron outputs zero on C_2 and is linear on C_1 , creating a piecewise linear function. For smooth activations, the partition marks regions of different qualitative behavior. The nerve complex $\mathcal{N}(\mathcal{P})$ of this partition is elementary: two vertices v_1, v_2 corresponding to the two cells, connected by a single edge since the cells share the boundary $H \cap \mathcal{D}$. The Riemannian structure

$$\langle \cdot, \cdot \rangle_{\mathcal{N}(\mathcal{P})} = \{ \langle \cdot, \cdot \rangle_{v_1}, \langle \cdot, \cdot \rangle_{v_2}, \langle \cdot, \cdot \rangle_{v_1 \wedge v_2} \}$$

over $\mathcal{N}(\mathcal{P})$ has the structure

$$\langle v_i, v_i \rangle_{v_i} = \text{vol}_n(C_i) \text{ for } i = 1, 2.$$

and

$$\langle v_1 \wedge v_2, v_1 \wedge v_2 \rangle_{v_1 \wedge v_2} = \text{vol}_{n-1}(C_1 \cap C_2) = \text{vol}_{n-1}(H \cap \mathcal{D})$$

The triple

$$(\mathcal{N}(\mathcal{P}), \langle \cdot, \cdot \rangle_{\mathcal{N}(\mathcal{P})}, \mathcal{F})$$

is the enriched simplicial complex associated with the partition \mathcal{P} and the local prediction functions \mathcal{F} .

When we combine m perceptrons into a single layer, the geometric structure becomes richer. The mapping $\rho : \mathcal{D} \rightarrow \mathbb{R}^m$ defined by

$$\rho(x) = (\sigma(w_1^T x + b_1), \dots, \sigma(w_m^T x + b_m)),$$

creates m hyperplanes that partition \mathcal{D} into cells [60]. Each cell corresponds to an activation pattern $\alpha \in \{0, 1\}^m$, indicating which neurons are active. Formally, the cell associated with pattern α is

$$C_\alpha = \bigcap_{j:\alpha_j=1} H_j^+ \cap \bigcap_{j:\alpha_j=0} H_j^- \cap \mathcal{D}.$$

This construction reveals an interesting connection to existing partition models. A layer of ReLU neurons can be viewed as an enrichment of Multivariate Adaptive Regression Splines (MARS) [31], where the axis-aligned hinge functions $(x^{(j)} - t)_+$ are replaced by arbitrarily oriented hyperplanes with ReLU activations $(\mathbf{w}^T x + b)_+$. Similarly, it generalizes oblique decision trees by replacing their discrete splits with continuous activation functions.

To illustrate how multiple neurons create richer geometric structures, consider a single layer neural network of two neurons with two inputs

$$\rho(x_1, x_2) = \begin{pmatrix} \sigma(2x_1 - x_2 - 0.5) \\ \sigma(-x_1 + 2x_2 - 0.5) \end{pmatrix}$$

operating on $\mathcal{D} = [0, 1]^2$. We present this example in detail to demonstrate both the partition structure and the induced Riemannian geometry.

The first neuron activates when $2x_1 - x_2 > 0.5$, creating the hyperplane

$$H_1 : 2x_1 - x_2 = 0.5.$$

The second neuron activates when $-x_1 + 2x_2 > 0.5$, creating the hyperplane

$$H_2 : -x_1 + 2x_2 = 0.5.$$

These two lines intersect at $(0.5, 0.5)$, creating a partition \mathcal{P} of \mathcal{D} with four cells:

$$\begin{aligned}
C_{00} &= \{(x_1, x_2) \in \mathcal{D} : 2x_1 - x_2 \leq 0.5 \text{ and } -x_1 + 2x_2 \leq 0.5\} \\
C_{01} &= \{(x_1, x_2) \in \mathcal{D} : 2x_1 - x_2 \leq 0.5 \text{ and } -x_1 + 2x_2 > 0.5\} \\
C_{10} &= \{(x_1, x_2) \in \mathcal{D} : 2x_1 - x_2 > 0.5 \text{ and } -x_1 + 2x_2 \leq 0.5\} \\
C_{11} &= \{(x_1, x_2) \in \mathcal{D} : 2x_1 - x_2 > 0.5 \text{ and } -x_1 + 2x_2 > 0.5\}
\end{aligned}$$

corresponding to the activation patterns, where we use subscript ij as shorthand for the pattern (i, j) .

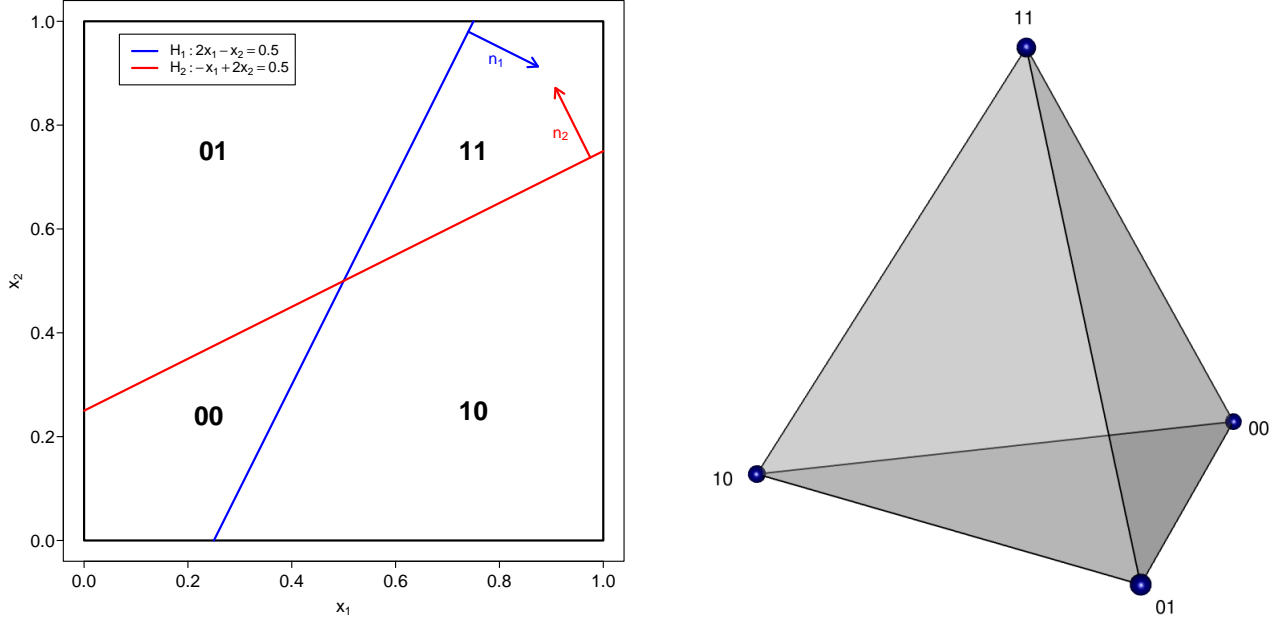


Figure 1: Partition \mathcal{P} induced by a two-neuron layer on the unit square. Left: The hyperplanes H_1 (blue) and H_2 (red) divide the domain into four cells C_{00} , C_{01} , C_{10} , and C_{11} corresponding to different activation patterns. Right: The nerve complex $\mathcal{N}(\mathcal{P})$ of this partition forms a 3-simplex simplicial complex since all four cells have a non-empty intersection.

The nerve complex $\mathcal{N}(\mathcal{P})$ of the partition \mathcal{P} forms a 3-simplex simplicial complex since all four cells have a non-empty intersection. In particular, the simplicial complex $\mathcal{N}(\mathcal{P})$ has the vertices: $\{v_{00}, v_{01}, v_{10}, v_{11}\}$ corresponding to the cells $\{C_{00}, C_{01}, C_{10}, C_{11}\}$ and it has six edges

$$\begin{aligned}
e_1 &= v_{00} \wedge v_{01}, \quad e_2 = v_{00} \wedge v_{10}, \quad e_3 = v_{01} \wedge v_{11} \\
e_4 &= v_{10} \wedge v_{11}, \quad e_5 = v_{00} \wedge v_{11}, \quad e_6 = v_{01} \wedge v_{10}
\end{aligned}$$

corresponding to faces

$$\begin{aligned}
F_1 &= C_{00} \cap C_{01} = H_1 \cap \{x_2 \leq 0.5\} \\
F_2 &= C_{00} \cap C_{10} = H_2 \cap \{x_1 \leq 0.5\} \\
F_3 &= C_{01} \cap C_{11} = H_2 \cap \{x_1 \geq 0.5\} \\
F_4 &= C_{10} \cap C_{11} = H_1 \cap \{x_2 \geq 0.5\} \\
F_5 &= C_{00} \cap C_{11} = \{(0.5, 0.5)\} \\
F_6 &= C_{01} \cap C_{10} = \{(0.5, 0.5)\}.
\end{aligned}$$

Moreover, it has four 2D simplicies corresponding to the four triples of four cells and it has one 3D simplex corresponding to the intersection $\{(0.5, 0.5)\}$ of the four cells.

For each pair of edges with 1D face (thus for edges e_1 to e_4) the edge inner product is

$$\langle e_i, e_j \rangle = \sqrt{\text{vol}_1(F_i) \cdot \text{vol}_1(F_j)} \cdot \cos \theta_{ij}$$

where $\text{vol}_1(F_i), \text{vol}_1(F_j)$ are the lengths of F_i and F_j faces and θ_{ij} is the interior dihedral angle between F_i and F_j within the corresponding cell. For example, the edges $e_1 = v_{00} \wedge v_{01}$ and $e_2 = v_{00} \wedge v_{10}$ correspond to faces F_1 and F_2 with the inner product

$$\langle e_1, e_2 \rangle_{v_{00}} = \sqrt{\text{vol}_1(F_1) \cdot \text{vol}_1(F_2)} \cdot \cos \theta_{12}$$

where

$$\cos \theta_{12} = \frac{\mathbf{n}_1 \cdot \mathbf{n}_2}{|\mathbf{n}_1| |\mathbf{n}_2|} = \frac{4}{5}$$

with the normal vectors $\mathbf{n}_1 = (2, -1)$ and $\mathbf{n}_2 = (1, -2)$ chosen so that \mathbf{n}_1 faces away from the cell C_{00} and \mathbf{n}_2 faces into it. This non-zero off-diagonal term creates a non-diagonal Gram matrix at vertex v_{00} , demonstrating that even a simple two-neuron feed-forward network exhibits genuinely non-trivial Riemannian structure.

This example illustrates how neural networks create geometric structures that connect to classical partition-based methods in machine learning. The hyperplanes divide the domain into regions with distinct computational behaviors, while the nerve complex and its Riemannian structure capture both the combinatorial relationships and the geometric configurations of these regions.

The true complexity emerges when we stack multiple layers. A feed-forward neural network with L layers defines a sequence of transformations:

$$\mathcal{D}_0 \xrightarrow{\rho_1} \mathcal{D}_1 \xrightarrow{\rho_2} \dots \xrightarrow{\rho_{L-1}} \mathcal{D}_{L-1} \xrightarrow{\rho_L} \mathbb{R}^m,$$

where $\mathcal{D}_0 = \mathcal{D}$ is our initial domain and $\mathcal{D}_\ell = \rho_\ell(\mathcal{D}_{\ell-1})$ for each subsequent layer. Each domain \mathcal{D}_ℓ carries a partition \mathcal{P}_ℓ induced by the hyperplanes of layer $\ell + 1$, giving rise to a sequence of nerve complexes

$$\mathcal{N}(\mathcal{P}_0), \mathcal{N}(\mathcal{P}_1), \dots, \mathcal{N}(\mathcal{P}_{L-1}).$$

Ideally, we would like each layer mapping ρ_ℓ to induce a well-defined map between the nerve complexes that preserves their structure. Such a map should send each vertex (cell) in the source complex to a vertex (cell) in the target complex, and preserve adjacency relationships: if two cells are adjacent in layer $\ell - 1$, their images should be adjacent or coincide in layer ℓ . More generally, if a collection of cells forms a simplex (all cells have a common intersection), their images should also form a simplex. Formally, a simplicial map $f : K \rightarrow L$ between simplicial complexes is a function on vertices $f : K_0 \rightarrow L_0$ such that whenever $\{v_0, v_1, \dots, v_k\} \in K$ forms a k -simplex, the image vertices $\{f(v_0), f(v_1), \dots, f(v_k)\}$ span a simplex in L (possibly of lower dimension if some vertices have the same image).

However, the mapping $\rho_\ell : \mathcal{D}_{\ell-1} \rightarrow \mathcal{D}_\ell$ does not naturally induce such a simplicial map between the nerve complexes, because a cell $C_\alpha^{\ell-1}$ from partition $\mathcal{P}_{\ell-1}$ maps under ρ_ℓ to a

set that may intersect multiple cells of partition \mathcal{P}_ℓ . There is no well-defined way to assign $C_\alpha^{\ell-1}$ to a single cell in the target partition.

To resolve this issue, we refine the partition $\mathcal{P}_{\ell-1}$ by subdividing each cell according to how it maps into cells of \mathcal{P}_ℓ . For each pair of cells $(C_\alpha^{\ell-1}, C_\beta^\ell)$ such that $\rho_\ell(C_\alpha^{\ell-1}) \cap C_\beta^\ell \neq \emptyset$, we define the refined cell

$$Q_{\alpha,\beta}^{\ell-1} = C_\alpha^{\ell-1} \cap \rho_\ell^{-1}(C_\beta^\ell).$$

Since ρ_ℓ is piecewise affine, these refined cells are polyhedra that partition the domain $\mathcal{D}_{\ell-1}$. The collection of all such refined cells forms a partition $\mathcal{P}_{\ell-1}^{\rho_\ell}$ of $\mathcal{D}_{\ell-1}$. By construction, each refined cell $Q_{\alpha,\beta}^{\ell-1}$ maps under ρ_ℓ entirely into a single cell C_β^ℓ of \mathcal{P}_ℓ . This induces a simplicial map

$$\hat{\rho}_\ell : K_{\rho_\ell}^{(\ell-1)} \rightarrow K^{(\ell)}$$

sending each vertex corresponding to $Q_{\alpha,\beta}^{\ell-1}$ to the vertex corresponding to C_β^ℓ , where $K_{\rho_\ell}^{(\ell-1)} = \mathcal{N}(\mathcal{P}_{\ell-1}^{\rho_\ell})$ and $K^{(\ell)} = \mathcal{N}(\mathcal{P}_\ell)$ (see Appendix B for the complete construction and verification).

The refined simplicial complex $K_{\rho_\ell}^{(\ell-1)}$ has vertices $v_{\alpha,\beta}^{\ell-1}$ corresponding to polytopes $Q_{\alpha,\beta}^{\ell-1}$. The simplicial complex structure of $K_{\rho_\ell}^{(\ell-1)}$ emerges naturally through the nerve of the the partition $\mathcal{P}_{\ell-1}^{\rho_\ell}$ construction: vertices connect by edges when their corresponding polytopes share a facet, triangles form when three polytopes meet along an edge, and higher-dimensional simplices arise from polytopes meeting at lower-dimensional faces. This construction captures the full combinatorial complexity of how the refined partition cells fit together.

Crucially, this refinement preserves functional information. Over each refined polytope $Q_{\alpha,\beta}^{\ell-1}$, the layer ℓ implements an affine map $f_{\alpha,\beta}^{\ell-1}(x) = W_{\alpha,\beta}^{\ell-1}x + b_{\alpha,\beta}^{\ell-1}$, where $W_{\alpha,\beta}^{\ell-1}$ is the weight matrix W_ℓ with rows corresponding to inactive neurons (according to pattern α) set to zero. This functional enrichment is fundamental: each vertex in our simplicial complex carries not just cell adjacency information but also the precise affine transformation applied to data in that region.

Having established the existence of refined partitions and their associated simplicial complexes, we now turn to the practical question of computing their Riemannian structure.

This geometric structure can be systematically computed using differential forms and pull-back operations. For each cell C_β^ℓ in layer ℓ , we associate the n -form ω_β defined by integration over the cell. The volume of the refined cell is then:

$$\text{vol}_n(Q_{\alpha,\beta}^{\ell-1}) = \left| \int_{C_\alpha^{\ell-1}} \rho_\ell^* \omega_\beta \right|$$

Since ρ_ℓ is affine on $C_\alpha^{\ell-1}$ with constant Jacobian matrix W_α , this simplifies to:

$$\text{vol}_n(Q_{\alpha,\beta}^{\ell-1}) = |\det(W_\alpha)| \cdot \text{vol}_n(W_\alpha^{-1}(C_\beta^\ell - b_\alpha) \cap C_\alpha^{\ell-1})$$

This pullback approach extends naturally to higher-dimensional chains. For edges in the refined complex, boundary volumes are computed by pulling back the appropriate $(n-1)$ -forms, providing a systematic method to build the complete Riemannian structure.

Given a finite dataset $X = \{x_1, \dots, x_N\} \subset \mathcal{D}$ with associated responses $y : X \rightarrow \mathbb{R}^m$, the feed-forward network learns an approximation to the conditional expectation of y given X . To properly track geometric information through the network while maintaining simplicial maps, we must work backwards from the final layer. This backward construction is necessary because the composition $\rho_L \circ \dots \circ \rho_1$ determines which cells in the input space map to the same final output region. By starting with the final partition and progressively refining earlier layers to respect these identifications, we ensure that all intermediate simplicial maps are well-defined.

This yields the sequence of simplicial complexes and maps:

$$K_{\rho_L, \dots, \rho_1}^{(0)} \xrightarrow{\hat{\rho}_1} K_{\rho_L, \dots, \rho_2}^{(1)} \xrightarrow{\hat{\rho}_2} \dots \xrightarrow{\hat{\rho}_{L-1}} K_{\rho_L}^{(L-1)} \xrightarrow{\hat{\rho}_L} K^{(L)}$$

where each $K_{\rho_L, \dots, \rho_{\ell+1}}^{(\ell)}$ is the nerve complex of the data-containing cells in the partition of \mathcal{D}_ℓ induced by the composition $\rho_L \circ \dots \circ \rho_{\ell+1}$. Specifically, we only include cells that contain the image under $\rho_\ell \circ \dots \circ \rho_1$ of at least one data point from X . The crucial observation is that each complex in this sequence is sufficiently refined to ensure that $\hat{\rho}_\ell$ is a well-defined simplicial map.

The enriched Riemannian simplicial complex structure associated with the feed-forward network consists of this entire sequence, not just the initial complex. While the first element

$$\left(K_{\rho_L, \dots, \rho_2, \rho_1}^{(0)}, \langle \cdot, \cdot \rangle_{K_{\rho_L, \dots, \rho_2, \rho_1}^{(0)}}, \mathcal{F}_{\rho_L, \dots, \rho_2, \rho_1}^{(0)} \right)$$

captures the final geometric structure induced on the data-supporting region of the input domain, the complete characterization requires the entire sequence of complexes together with the simplicial maps between them. Here, $\langle \cdot, \cdot \rangle_{K_{\rho_L, \dots, \rho_2, \rho_1}^{(0)}}$ is the Riemannian structure derived from the data-containing cells of the partition of \mathcal{D} , and $\mathcal{F}_{\rho_L, \dots, \rho_2, \rho_1}^{(0)}$ consists of the restrictions of the full network function $\rho_L \circ \dots \circ \rho_1$ to each such cell.

This sequential perspective reveals the true richness of the neural network's geometric structure. Each simplicial map $\hat{\rho}_\ell$ tracks how geometric information propagates through layer ℓ , while the sequence as a whole captures how the network progressively refines its partition of the input space. This allows us to define invariants that utilize the entire construction process, not just the final result. For instance, we can track how the dimensions of simplices evolve through the sequence, measure the distortion introduced by each layer map, or analyze how the Riemannian structure changes as information flows through the network.

The differential forms framework provides a systematic approach to computing the Riemannian structure. For the 0-chain structure, each vertex $v_{\alpha, \beta}$ in the refined complex has inner product:

$$\langle v_{\alpha, \beta}, v_{\alpha, \beta} \rangle_0 = \text{vol}_n(Q_{\alpha, \beta}^{\ell-1})$$

computed via the pullback formula above. For 1-chains, consider edges $e = v_{\alpha, \beta} \wedge v_{\alpha', \beta'}$. The boundary $F = \overline{Q_{\alpha, \beta}^{\ell-1}} \cap \overline{Q_{\alpha', \beta'}^{\ell-1}}$ has $(n-1)$ -dimensional volume that can be computed by pulling back the appropriate boundary forms.

This approach extends naturally to compositions of layers. For a deep network $\rho_L \circ \dots \circ \rho_1$, we work backwards from the final partition, computing volumes via composed pullbacks:

$$\text{vol}_n(Q^{(0)}) = \left| \int_{C^{(0)}} (\rho_1^* \circ \rho_2^* \circ \dots \circ \rho_L^*) \omega_{\text{final}} \right|$$

The differential forms framework provides a path forward for computing this Riemannian structure. Rather than viewing the refined cells as intractable geometric objects, we can leverage the fact that volumes and boundary measures transform systematically under pullback. For practical implementation, we need only track cells containing training data and compute their volumes via composed pullbacks. The geometric regularization methods developed in Section 2 can then be applied using these computed volumes and boundary measures, potentially leading to networks with more interpretable decision boundaries, better generalization properties, and improved robustness.

This geometric perspective transforms neural networks from opaque function approximators into mathematically precise geometric objects. The key insight is that neural networks implement functionally enriched structures where each layer creates both a simplicial complex encoding partition topology and a collection of affine maps specifying local computations. The differential forms approach makes this dual structure computationally accessible: the pullback operation systematically tracks how volumes, angles, and other geometric quantities transform through the network.

The framework extends naturally beyond ReLU networks. For smooth activation functions like sigmoid or tanh, the layer maps ρ_ℓ are smooth rather than piecewise affine. The pullback of forms remains well-defined:

$$(\rho_\ell^* \omega)(x) = \omega(\rho_\ell(x)) \cdot \det(J_{\rho_\ell}(x)),$$

where $J_{\rho_\ell}(x)$ is the Jacobian matrix at point x . While smooth activations don't create discrete partitions, we can use data-induced partitions (such as Voronoi cells from training points) and apply the pullback formalism to compute induced volumes. The varying Jacobian creates a naturally curved Riemannian geometry that captures how the network distorts space continuously rather than through discrete cells. For attention mechanisms in Transformers, the data-dependent partitions created by attention patterns fit naturally into this framework, with attention weights providing additional geometric structure.

In practice, several strategies make implementation feasible. We need only track cells containing training data, reducing complexity from potentially exponential in the number of neurons to linear in the number of training examples. During forward propagation, recording activation patterns identifies which refined cells actually influence model behavior. For ReLU networks with affine maps $\rho_\ell(x) = W_\alpha x + b_\alpha$ on each cell, the pullback formulas provide explicit volume computations through the Jacobian determinant $|\det(W_\alpha)|$.

The differential forms framework also suggests new theoretical questions bridging abstract mathematics and practical machine learning. Can we characterize which architectures maintain tractable geometric structures under pullback? How does the condition number of Jacobian matrices relate to generalization? What geometric invariants predict model robustness? These questions open avenues for both theoretical advances and practical tools for analyzing neural networks.

While challenges remain in scaling these computations to very large networks, the systematic nature of the pullback formalism provides a principled path forward. The intersection of discrete geometry with deep learning offers rich opportunities for developing new regularization methods, interpretability tools, and architectural insights grounded in rigorous mathematical foundations.

Appendix A: Derivation of the Whitney Extension Formula

We establish that both the Whitney extension and harmonic extension of a vertex function to p -simplices yield the same formula, namely the barycentric average weighted by simplex volume. Consider a p -simplex $\sigma = [v_0, v_1, \dots, v_p]$ in a Riemannian simplicial complex K . The Riemannian structure determines edge lengths $\ell_{ij} = d(v_i, v_j)$ for all vertex pairs, where the distance function d is induced by the Riemannian metric on the 1-skeleton of K . These edge lengths allow us to embed σ isometrically into Euclidean space \mathbb{R}^{p+1} using the Cayley-Menger construction [11, 9], establishing a concrete geometric realization that preserves all distance relationships.

For the embedded simplex, we introduce barycentric coordinates $(\lambda_0, \lambda_1, \dots, \lambda_p)$ such that any point $x \in \sigma$ can be uniquely expressed as $x = \sum_{i=0}^p \lambda_i v_i$ where $\lambda_i \geq 0$ and $\sum_{i=0}^p \lambda_i = 1$. These coordinates provide a natural parametrization of the simplex that respects its affine structure [22]. The constraint $\sum_{i=0}^p \lambda_i = 1$ implies that only p of these coordinates are independent; we may express $\lambda_0 = 1 - \sum_{j=1}^p \lambda_j$ and use $(\lambda_1, \dots, \lambda_p)$ as free parameters ranging over the standard p -simplex in parameter space.

The Whitney extension formula for lifting a vertex function $u : V(K) \rightarrow \mathbb{R}$ to a p -cochain is given by [72]

$$\kappa_p^{\text{Whitney}}(u)(\sigma) = \sum_{i=0}^p u(v_i) \int_{\sigma} \lambda_i d\lambda_0 \wedge \dots \wedge \widehat{d\lambda_i} \wedge \dots \wedge d\lambda_p$$

where the hat indicates omission of the corresponding differential. To evaluate these integrals, we first observe that due to the linear constraint among barycentric coordinates, we have $d\lambda_0 = -\sum_{j=1}^p d\lambda_j$. This relationship allows us to express any differential form involving $d\lambda_0$ in terms of the independent differentials $d\lambda_1, \dots, d\lambda_p$.

Consider the integral $\int_{\sigma} \lambda_i d\lambda_0 \wedge \dots \wedge \widehat{d\lambda_i} \wedge \dots \wedge d\lambda_p$. When $i = 0$, we have

$$\int_{\sigma} \lambda_0 d\lambda_1 \wedge \dots \wedge d\lambda_p = \int_{\sigma} \left(1 - \sum_{j=1}^p \lambda_j\right) d\lambda_1 \wedge \dots \wedge d\lambda_p$$

For $i \geq 1$, substituting $d\lambda_0 = -\sum_{j=1}^p d\lambda_j$ into the differential form and using the antisymmetry of the wedge product, we find that

$$d\lambda_0 \wedge d\lambda_1 \wedge \dots \wedge \widehat{d\lambda_i} \wedge \dots \wedge d\lambda_p = (-1)^i d\lambda_1 \wedge \dots \wedge d\lambda_p$$

Thus all integrals reduce to computing $\int_{\sigma} \lambda_i dV_{\sigma}$, where dV_{σ} represents the volume element on the p -dimensional simplex. By the symmetry of the simplex under permutations of vertices, each barycentric coordinate has the same integral value. Since $\sum_{i=0}^p \lambda_i = 1$ identically on σ , we have

$$(p+1) \int_{\sigma} \lambda_i dV_{\sigma} = \int_{\sigma} \sum_{i=0}^p \lambda_i dV_{\sigma} = \int_{\sigma} 1 dV_{\sigma} = \text{vol}_p(\sigma)$$

Therefore, $\int_{\sigma} \lambda_i dV_{\sigma} = \text{vol}_p(\sigma)/(p+1)$ for each i . This classical result about the integral of barycentric coordinates over a simplex can be found in [44] and follows from the fact that the barycenter divides the simplex into $p+1$ equal-volume parts. Thus we obtain

$$\kappa_p^{\text{Whitney}}(u)(\sigma) = \sum_{i=0}^p u(v_i) \cdot \frac{\text{vol}_p(\sigma)}{p+1} = \frac{\text{vol}_p(\sigma)}{p+1} \sum_{i=0}^p u(v_i)$$

For the harmonic extension approach, we seek a function $H : \sigma \rightarrow \mathbb{R}$ that minimizes the Dirichlet energy $\int_{\sigma} \|\nabla H\|^2 dV_{\sigma}$ subject to the boundary conditions $H(v_i) = u(v_i)$ for all vertices. The Euler-Lagrange equation for this variational problem is Laplace's equation $\Delta H = 0$ on the interior of σ [29]. Since σ is a simplex, the solution is the unique affine function interpolating the vertex values, namely $H(x) = \sum_{i=0}^p \lambda_i(x)u(v_i)$. This can be verified directly: the barycentric coordinates λ_i are affine functions of the Cartesian coordinates, hence their second derivatives vanish, giving $\Delta H = \sum_{i=0}^p u(v_i)\Delta\lambda_i = 0$.

The p -cochain value is then obtained by integrating this harmonic function:

$$\kappa_p^{\text{harm}}(u)(\sigma) = \int_{\sigma} H dV_{\sigma} = \int_{\sigma} \sum_{i=0}^p \lambda_i u(v_i) dV_{\sigma} = \sum_{i=0}^p u(v_i) \int_{\sigma} \lambda_i dV_{\sigma}$$

Using our previous calculation, this yields

$$\kappa_p^{\text{harm}}(u)(\sigma) = \frac{\text{vol}_p(\sigma)}{p+1} \sum_{i=0}^p u(v_i)$$

Thus both the Whitney extension and harmonic extension produce the same lifted values, demonstrating that the formula represents a fundamental geometric property of simplicial interpolation. The volume $\text{vol}_p(\sigma)$ appearing in this formula is determined by the Riemannian structure through the edge lengths. For a p -simplex with edge lengths $\{\ell_{ij}\}_{0 \leq i < j \leq p}$, the volume can be computed using the Cayley-Menger determinant [9]:

$$\text{vol}_p(\sigma)^2 = \frac{(-1)^{p+1}}{2^p(p!)^2} \begin{vmatrix} 0 & 1 & 1 & \cdots & 1 \\ 1 & 0 & \ell_{01}^2 & \cdots & \ell_{0p}^2 \\ 1 & \ell_{01}^2 & 0 & \cdots & \ell_{1p}^2 \\ \vdots & \vdots & \vdots & \ddots & \vdots \\ 1 & \ell_{0p}^2 & \ell_{1p}^2 & \cdots & 0 \end{vmatrix}$$

This completes the derivation, showing that the lifted value on any p -simplex equals the volume-weighted barycentric average of the vertex values, with the volume determined by the Riemannian structure of the simplicial complex.

Appendix B: Construction of Simplicial Maps Between Neural Network Layers

This appendix provides the rigorous construction of simplicial maps between consecutive layers of a neural network, complementing the differential forms framework introduced in Section 3. While Section 3 showed how to compute the Riemannian structure via pullback operations, here we establish the foundational result that well-defined simplicial maps exist between the nerve complexes of consecutive layers.

Consider a feed-forward neural network with layer mappings $\rho_\ell : \mathbb{R}^{n_{\ell-1}} \rightarrow \mathbb{R}^{n_\ell}$. As established in Section 2.2, each ReLU layer induces a polyhedral partition of its input space. The challenge is that when a cell from layer $\ell - 1$ maps forward under ρ_ℓ , its image typically intersects multiple cells in layer ℓ 's partition, so ρ_ℓ does not directly induce a simplicial map between the nerve complexes.

We resolve this through a refinement procedure. Given partitions $\mathcal{P}_{\ell-1} = \{C_\alpha^{\ell-1}\}$ and $\mathcal{P}_\ell = \{C_\beta^\ell\}$, we define the refined partition consisting of cells:

$$Q_{\alpha,\beta}^{\ell-1} = C_\alpha^{\ell-1} \cap \rho_\ell^{-1}(C_\beta^\ell)$$

Lemma 1. *The collection $\mathcal{Q}_{\ell-1} = \{Q_{\alpha,\beta}^{\ell-1} : Q_{\alpha,\beta}^{\ell-1} \neq \emptyset\}$ forms a partition of $\mathcal{D}_{\ell-1}$.*

Proof. We verify coverage and disjointness. For coverage, any $x \in \mathcal{D}_{\ell-1}$ belongs to some $C_\alpha^{\ell-1}$ and $\rho_\ell(x)$ belongs to some C_β^ℓ , hence $x \in Q_{\alpha,\beta}^{\ell-1}$. For disjointness, if $x \in Q_{\alpha,\beta}^{\ell-1} \cap Q_{\alpha',\beta'}^{\ell-1}$, then $x \in C_\alpha^{\ell-1} \cap C_{\alpha'}^{\ell-1}$ implies $\alpha = \alpha'$, and $\rho_\ell(x) \in C_\beta^\ell \cap C_{\beta'}^\ell$ implies $\beta = \beta'$. \square

Each refined cell remains a convex polyhedron since ρ_ℓ is affine on $C_\alpha^{\ell-1}$ with $\rho_\ell(x) = W_\alpha x + b_\alpha$. The volume of the refined cell, as shown in Section 3, is computed via the pullback formula:

$$\text{vol}_n(Q_{\alpha,\beta}^{\ell-1}) = |\det(W_\alpha)| \cdot \text{vol}_n(W_\alpha^{-1}(C_\beta^\ell - b_\alpha) \cap C_\alpha^{\ell-1})$$

Theorem 2. *The map $\hat{\rho}_\ell : K_{\text{ref}}^{(\ell-1)} \rightarrow K^{(\ell)}$ defined by $\hat{\rho}_\ell(v_{\alpha,\beta}) = v_\beta$ on vertices and extended linearly to simplices is a well-defined simplicial map.*

Proof. Let $\sigma = [v_{\alpha_0,\beta_0}, \dots, v_{\alpha_k,\beta_k}]$ be a simplex in $K_{\text{ref}}^{(\ell-1)}$. By definition, $\bigcap_{i=0}^k Q_{\alpha_i,\beta_i}^{\ell-1} \neq \emptyset$. For any x in this intersection, we have $\rho_\ell(x) \in \bigcap_{i=0}^k C_{\beta_i}^\ell$, which is non-empty. Therefore the vertices $\{v_{\beta_i}\}$ span a simplex in $K^{(\ell)}$. Face relations are preserved since faces of σ map to faces of $\hat{\rho}_\ell(\sigma)$. \square

The construction satisfies functorial properties: identity maps induce identity simplicial maps, and the diagram for composed layer maps commutes after appropriate refinements.

For deep networks, the backward construction from Section 3.1 ensures compatibility across all layers. Starting from the final partition induced by $\rho_L \circ \dots \circ \rho_1$, we progressively refine earlier partitions to obtain the sequence:

$$K_{\rho_L, \dots, \rho_1}^{(0)} \xrightarrow{\hat{\rho}_1} K_{\rho_L, \dots, \rho_2}^{(1)} \xrightarrow{\hat{\rho}_2} \dots \xrightarrow{\hat{\rho}_L} K^{(L)}$$

The differential forms framework from Section 3 shows how to compute the Riemannian structure on these complexes through systematic pullback calculations. The Jacobian matrices W_α that appear in the volume formula above are precisely the local linear approximations that determine how geometric quantities transform under the layer mappings.

This completes the rigorous foundation for analyzing neural networks as sequences of simplicial complexes with well-defined maps between them, while the computational aspects are handled through the differential forms machinery developed in the main text.

References

- [1] Rolf Adams and Leanne Bischof. Seeded region growing. *IEEE Transactions on Pattern Analysis and Machine Intelligence*, 16(6):641–647, 1994.
- [2] Guillaume Alain and Yoshua Bengio. Understanding intermediate layers using linear classifier probes. In *International Conference on Learning Representations*, 2017.
- [3] Shun-ichi Amari. *Information Geometry and Its Applications*, volume 194 of *Applied Mathematical Sciences*. Springer, Tokyo, 2016.
- [4] Vladimir I Arnold. Sur la géométrie différentielle des groupes de Lie de dimension infinie et ses applications à l’hydrodynamique des fluides parfaits. *Annales de l’Institut Fourier*, 16(1):319–361, 1966.
- [5] Franz Aurenhammer. Voronoi diagrams—a survey of a fundamental geometric data structure. *ACM Computing Surveys*, 23(3):345–405, 1991.
- [6] Peter L Bartlett and Shahar Mendelson. Rademacher and gaussian complexities: Risk bounds and structural results. *Journal of Machine Learning Research*, 3:463–482, 2002.
- [7] Yonatan Belinkov and James Glass. Analysis methods in neural language processing: A survey. *Transactions of the Association for Computational Linguistics*, 6:49–72, 2017.
- [8] Kristin P. Bennett and Colin Campbell. A linear programming approach to novelty detection. In *Advances in Neural Information Processing Systems*, pages 395–401, 2000.
- [9] Marcel Berger. *Geometry I*. Springer, corrected fourth printing edition, 2009. Section 9.7: The Cayley-Menger determinants.
- [10] Monica Bianchini and Franco Scarselli. On the complexity of neural network classifiers: A comparison between shallow and deep architectures. *IEEE Transactions on Neural Networks and Learning Systems*, 25(8):1553–1565, 2014.
- [11] Leonard M. Blumenthal. *Theory and Applications of Distance Geometry*. Clarendon Press, Oxford, 1953. Chapter IV provides comprehensive treatment of the Cayley-Menger determinant.

- [12] Karol Borsuk. On the imbedding of systems of compacta in simplicial complexes. *Fundamenta Mathematicae*, 35(1):217–234, 1948.
- [13] Raoul Bott and Loring W. Tu. *Differential Forms in Algebraic Topology*, volume 82 of *Graduate Texts in Mathematics*. Springer-Verlag, 1982.
- [14] Léon Bottou and Vladimir Vapnik. Local learning algorithms. *Neural Computation*, 4(6):888–900, 1992.
- [15] Glen E. Bredon. *Sheaf Theory*, volume 170 of *Graduate Texts in Mathematics*. Springer-Verlag, 2nd edition, 1997.
- [16] Leo Breiman. Random forests. *Machine learning*, 45(1):5–32, 2001.
- [17] Leo Breiman, Jerome H. Friedman, Richard A. Olshen, and Charles J. Stone. *Classification and Regression Trees*. Wadsworth International Group, Belmont, CA, 1984.
- [18] Michael M Bronstein, Joan Bruna, Yann LeCun, Arthur Szlam, and Pierre Vandergheynst. Geometric deep learning: going beyond euclidean data. *IEEE Signal Processing Magazine*, 34(4):18–42, 2017.
- [19] Gunnar Carlsson. Topology and data. *Bulletin of the American Mathematical Society*, 46(2):255–308, 2009.
- [20] William S Cleveland and Susan J Devlin. Locally weighted regression: an approach to regression analysis by local fitting. *Journal of the American Statistical Association*, 83(403):596–610, 1988.
- [21] Thomas Cover and Peter Hart. Nearest neighbor pattern classification. *IEEE Transactions on Information Theory*, 13(1):21–27, 1967.
- [22] Harold Scott MacDonald Coxeter. *Introduction to Geometry*. John Wiley & Sons, New York, 2nd edition, 1969. Chapter 13: Coordinates.
- [23] George Cybenko. Approximation by superpositions of a sigmoidal function. *Mathematics of control, signals and systems*, 2(4):303–314, 1989.
- [24] Boris Delaunay. Sur la sphère vide. *Bulletin de l'Académie des Sciences de l'URSS*, 6:793–800, 1934.
- [25] Mathieu Desbrun, Anil N Hirani, Melvin Leok, and Jerrold E Marsden. Discrete exterior calculus. *arXiv preprint math/0508341*, 2005.
- [26] Manfredo Perdigão do Carmo. *Riemannian geometry*. Mathematics: Theory & Applications. Birkhäuser, Boston, 1992.
- [27] Finale Doshi-Velez and Been Kim. Towards a rigorous science of interpretable machine learning. *arXiv preprint arXiv:1702.08608*, 2017.
- [28] Herbert Edelsbrunner and John Harer. Persistent homology—a survey. *Contemporary Mathematics*, 453:257–282, 2008.

- [29] Lawrence C. Evans. *Partial Differential Equations*, volume 19 of *Graduate Studies in Mathematics*. American Mathematical Society, Providence, RI, 2nd edition, 2010.
- [30] Herbert Federer. *Geometric Measure Theory*. Classics in Mathematics. Springer-Verlag, Berlin, Heidelberg, 1996. Reprint of the 1969 edition.
- [31] Jerome H. Friedman. Multivariate adaptive regression splines. *The Annals of Statistics*, 19(1):1–67, 1991.
- [32] Jerome H. Friedman. Greedy function approximation: a gradient boosting machine. *Annals of statistics*, pages 1189–1232, 2001.
- [33] Ian Goodfellow, Yoshua Bengio, and Aaron Courville. *Deep learning*. MIT press, 2016.
- [34] Robert M. Gray and David L. Neuhoff. Quantization. *IEEE Transactions on Information Theory*, 44(6):2325–2383, 1998.
- [35] Trevor Hastie, Robert Tibshirani, and Jerome Friedman. *The Elements of Statistical Learning: Data Mining, Inference, and Prediction*. Springer Series in Statistics. Springer, New York, 2 edition, 2009.
- [36] Allen Hatcher. *Algebraic topology*. Cambridge University Press, 2002.
- [37] David Heath, Simon Kasif, and Steven Salzberg. Induction of oblique decision trees. In *Proceedings of the 13th International Joint Conference on Artificial Intelligence*, pages 1002–1007, 1993.
- [38] Anil N. Hirani. *Discrete exterior calculus*. PhD thesis, California Institute of Technology, 2003.
- [39] Kurt Hornik, Maxwell Stinchcombe, and Halbert White. Multilayer feedforward networks are universal approximators. *Neural networks*, 2(5):359–366, 1989.
- [40] Arthur Jacot, Franck Gabriel, and Clément Hongler. Neural tangent kernel: Convergence and generalization in neural networks. In *Advances in neural information processing systems*, volume 31, 2018.
- [41] Jürgen Jost. *Riemannian Geometry and Geometric Analysis*. Springer, Berlin, 6 edition, 2011.
- [42] Masaki Kashiwara and Pierre Schapira. *Sheaves on Manifolds*, volume 292 of *Grundlehren der mathematischen Wissenschaften*. Springer-Verlag, 2003.
- [43] Teuvo Kohonen. *Learning vector quantization*. Self-Organizing Maps. Springer, Berlin, 2 edition, 1995.
- [44] Jean B. Lasserre. Integration on a simplex: A new proof of a result by Folland. *The American Mathematical Monthly*, 106(9):872–874, 1999.
- [45] Yann LeCun, Yoshua Bengio, and Geoffrey Hinton. Deep learning. *Nature*, 521(7553):436–444, 2015.

- [46] Jean Leray. Sur la forme des espaces topologiques et sur les points fixes des représentations. *Journal de Mathématiques Pures et Appliquées*, 24:95–167, 1945.
- [47] Hao Li, Zheng Xu, Gavin Taylor, Christoph Studer, and Tom Goldstein. Visualizing the loss landscape of neural nets. In *Advances in Neural Information Processing Systems*, volume 31. Curran Associates, Inc., 2018.
- [48] Mehryar Mohri, Afshin Rostamizadeh, and Ameet Talwalkar. *Foundations of machine learning*. MIT Press, Cambridge, MA, 2012.
- [49] James R Munkres. *Elements of algebraic topology*. CRC press, 1984.
- [50] Sreerama K. Murthy, Simon Kasif, and Steven Salzberg. A system for induction of oblique decision trees. In *Journal of Artificial Intelligence Research*, volume 2, pages 1–32, 1994.
- [51] Behnam Neyshabur, Srinadh Bhojanapalli, David McAllester, and Nathan Srebro. Exploring generalization in deep learning. In *Advances in Neural Information Processing Systems*, volume 30, pages 5947–5956, 2017.
- [52] Atsuyuki Okabe, Barry Boots, Kokichi Sugihara, and Sung Nok Chiu. *Spatial Tessellations: Concepts and Applications of Voronoi Diagrams*. John Wiley & Sons, 2nd edition, 2000.
- [53] Chris Olah, Alexander Mordvintsev, and Ludwig Schubert. Feature visualization. *Distill*, 2(11):e7, 2017.
- [54] Gabriel Peyré and Marco Cuturi. Computational optimal transport: With applications to data science. *Foundations and Trends in Machine Learning*, 11(5-6):355–607, 2019.
- [55] Ben Poole, Subhaneil Lahiri, Maithra Raghu, Jascha Sohl-Dickstein, and Surya Ganguli. Exponential expressivity in deep neural networks through transient chaos. *Advances in neural information processing systems*, 29, 2016.
- [56] Franco P. Preparata and Michael Ian Shamos. *Computational Geometry: An Introduction*. Springer-Verlag, New York, 1985.
- [57] Sam T. Roweis and Lawrence K. Saul. Nonlinear dimensionality reduction by locally linear embedding. *Science*, 290(5500):2323–2326, 2000.
- [58] Cynthia Rudin. Stop explaining black box machine learning models for high stakes decisions and use interpretable models instead. *Nature Machine Intelligence*, 1(5):206–215, 2019.
- [59] Noam Slonim and Naftali Tishby. Agglomerative information bottleneck. In *Advances in Neural Information Processing Systems*, volume 12, pages 617–623. MIT Press, 1999.
- [60] Richard P Stanley. An introduction to hyperplane arrangements. In Ezra Miller, Victor Reiner, and Bernd Sturmfels, editors, *Geometric Combinatorics*, volume 13 of *IAS/Park City Mathematics Series*, pages 389–496. American Mathematical Society, 2004.

- [61] Joshua B. Tenenbaum, Vin de Silva, and John C. Langford. A global geometric framework for nonlinear dimensionality reduction. *Science*, 290(5500):2319–2323, 2000.
- [62] Prasad Tetali. Random walks and the effective resistance of networks. *Journal of Theoretical Probability*, 4(1):101–109, 1991.
- [63] Robert Tibshirani. Regression shrinkage and selection via the lasso. *Journal of the Royal Statistical Society Series B: Statistical Methodology*, 58(1):267–288, 1996.
- [64] Vladimir N. Vapnik. *Statistical learning theory*. Wiley-Interscience, New York, 1998.
- [65] Vladimir N. Vapnik and Alexey Ya. Chervonenkis. On the uniform convergence of relative frequencies of events to their probabilities. *Theory of Probability & Its Applications*, 16(2):264–280, 1971.
- [66] Cédric Villani. *Topics in optimal transportation*, volume 58 of *Graduate Studies in Mathematics*. American Mathematical Society, 2003.
- [67] Georgy Voronoi. Nouvelles applications des paramètres continus à la théorie des formes quadratiques. *Journal für die reine und angewandte Mathematik*, 134:198–287, 1908.
- [68] Robert M Wald. *General Relativity*. University of Chicago Press, Chicago, 1984.
- [69] Frank W. Warner. *Foundations of Differentiable Manifolds and Lie Groups*, volume 94 of *Graduate Texts in Mathematics*. Springer-Verlag, 1983.
- [70] André Weil. Sur les théorèmes de de Rham. *Commentarii Mathematici Helvetici*, 26(1):119–145, 1952.
- [71] J.H.C. Whitehead. On C^1 -complexes. *Annals of Mathematics*, 41(4):809–824, 1940.
- [72] Hassler Whitney. *Geometric Integration Theory*. Princeton University Press, Princeton, NJ, 1957.
- [73] Chiyuan Zhang, Samy Bengio, Moritz Hardt, Benjamin Recht, and Oriol Vinyals. Understanding deep learning requires rethinking generalization. In *International Conference on Learning Representations*, 2017.
- [74] Heping Zhang and Burton Singer. Recursive partitioning in the health sciences. *Statistics for Biology and Health*, 1998.
- [75] Hui Zou and Trevor Hastie. Regularization and variable selection via the elastic net. *Journal of the Royal Statistical Society: Series B*, 67(2):301–320, 2005.